Research Square

Preprints are preliminary reports that have not undergone peer review.
They should not be considered conclusive, used to inform clinical practice,
or referenced by the media as validated information.

Torsional instability of the 1940 Tacoma Narrows Bridge: Critical wind speed and structural stress at prototype scale

Mingze Hong

hongmingze2006@gmail.com

Sichuan University https://orcid.org/0009-0001-3549-9396

Bojun Yang

Sichuan University https://orcid.org/0009-0006-9517-8742

Research Article

Keywords: bridge aeroelasticity, vortex shedding, torsional flutter, similitude, crack-band damage

Posted Date: November 25th, 2026

DOI: https://doi.org/10.21203/rs.3.rs-11859592/v1

License: This work is licensed under a Creative Commons Attribution 4.0 International License.
Read Full License

Additional Declarations: The authors declare no competing interests.

Torsional instability of the 1940 Tacoma Narrows Bridge

Critical wind speed and structural stress at prototype scale

Mingze Hong and Bojun Yang

Department of Mechanics Science and Engineering, College of Architecture and Environment, Sichuan University

四川大学建筑与环境学院力学科学与工程系

Mingze Hong | ORCID 0009-0001-3549-9396 | hongmingze2006@gmail.com

Bojun Yang | ORCID 0009-0006-9517-8742

Technical report | 24 November 2026

Abstract

This report estimates the wind speed at which the original Tacoma Narrows Bridge could enter a dangerous aeroelastic regime. We define its onset by zero total damping of small torsional motion. Independent studies support a prototype reference of 9.0 m/s, equivalent to 0.90 m/s at 1:100 Froude scale. A historical full-bridge wind-tunnel model gives a lower estimate of 7.1 m/s. The local wind readings on the day of failure do not identify the speed at first loss of damping. Models built with TENSORA v1.2.7 examine how wind loads act on the deck and reach its supports. The symmetric span admits the historical antisymmetric mode, although uniform sectional loading fails to excite it. At 18 m/s prototype-equivalent wind, the isolated two-bay segment gives a peak equivalent stress of 7.91 MPa at an idealized steel restraint. The prototype concrete patch reaches 0.01742 MPa in tension against its assumed 3 MPa tensile strength. These stresses describe a short loading history. The available runs establish neither a structural failure load nor a day-of-collapse stress field.

Keywords *bridge aeroelasticity · vortex shedding · torsional flutter · similitude · crack-band damage*

Contents

1–2 Historical observations and bridge geometry 2
3–4 Similitude, air loads and stability criteria 6
5–8 Section, segment, span and concrete patch models 10
9–10 Verification criteria and data sources 20
11 Numerical results, field histories and verification 23
12 Findings and engineering interpretation 48
12.2 Historical response checks 49
12.3 Prototype critical wind speed 50
12.4–12.5 Prototype stresses and local damage 51
References and data availability 53

1 Historical observations and testable mechanisms

On 7 November 1940, wind speed at the bridge was reported as 38 mph at 07:30 and 42 mph near the east end two hours later (17.0 and 18.8 m/s). The roadway began twisting at about 10:03. The local readings motivate the nominal 18 m/s prototype crosswind. The spanwise wind distribution during the transition is unknown [2].

Contemporary records place the early vertical motion near 0.60–0.63 Hz. Estimates for the later torsion range from about 0.20 to 0.23 Hz across accounts [3, 6, 9]. A periodic wake can synchronize with heave. Growth of torsion also requires the wind to replace the energy dissipated over a cycle. We therefore examine the fixed wake, the signed work on the moving section and the spatial distribution of moment as separate observables.

1.1 The engineering problem at three length scales

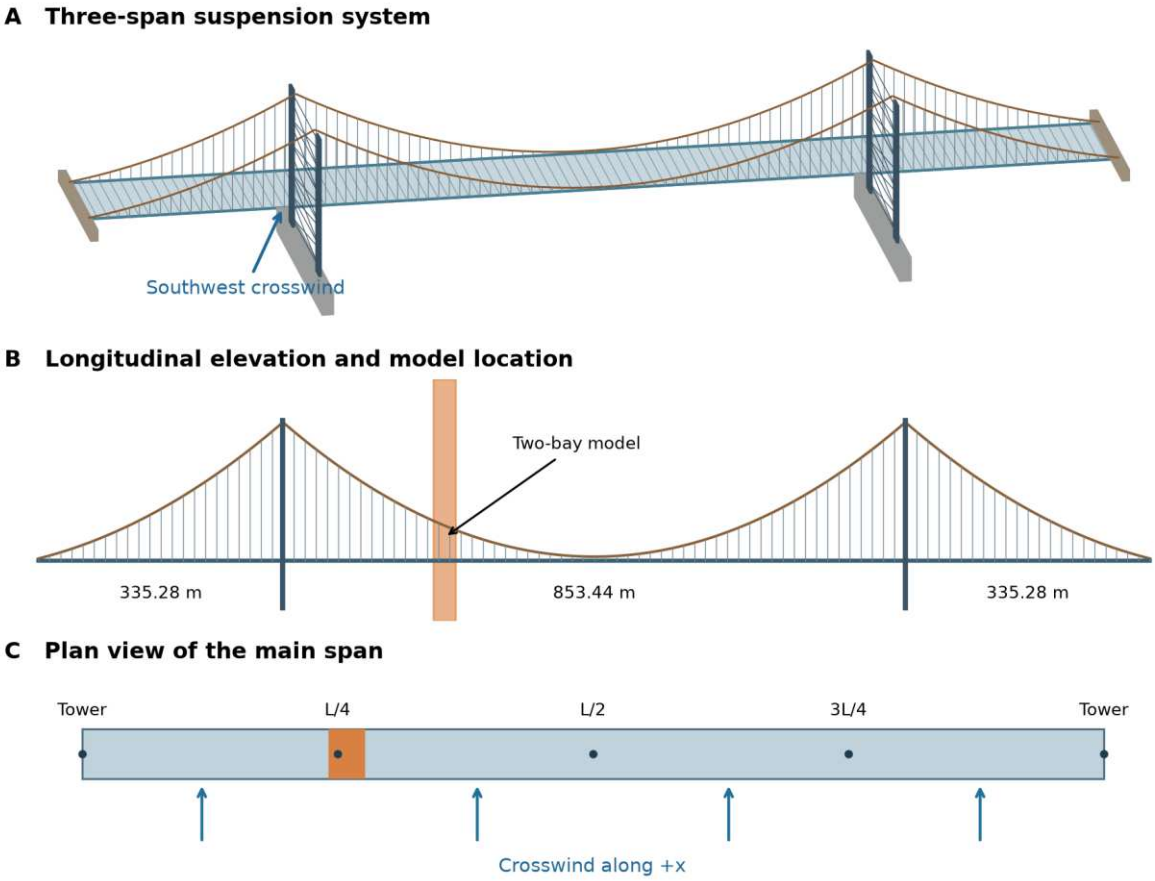

Figure 1. The engineering problem in spatial view, elevation and plan. Brown lines indicate the main cables. The colored interval is the independently modeled two-bay segment. The wind arrow denotes the transverse component used in the study. The plan exaggerates deck width for visibility.

The general-arrangement file contains the 335.28 m side spans, 853.44 m center span, roadway, two girder lines, main cables, grouped suspenders, floor beams, tower portals, piers and end anchorages [1]. Dimensions controlling the span lengths and nominal hanger spacing come from the historical inventory. Pier blocks, portal bracing, approach-cable profiles and anchorage solids are schematic. The file establishes the engineering context and permits rotation and component isolation.

Wind acts across the deck and drives pressure differences around the plate girders. Floor beams carry deck actions to the edges, and suspenders transmit them to the main cables. The two-bay solid occupies prototype stations 205.74–236.22 m from the first main-span tower. The first floor beam stands at L/4. A 1.20 m concrete patch is centered on the roadway there. The full-span tangent supplies the intermediate length scale needed to distinguish a local distortion from a global mode.

2 Geometry and evidence

The center span was 2,800 ft long. The 26 ft roadway, 39 ft cable spacing and 8 ft plate-girder depth describe different features [1]. Their distinction matters because the chosen reference width enters reduced velocity linearly and aerodynamic moment quadratically. The independent 2D flow geometry follows the idealized H-section in Song et al. [3, Fig. 1 and Table 1]. Its 12 m overall width and equivalent deck thickness provide a reproducible comparison with their flow study.

Table 1. Geometric inputs. The aerodynamic plates represent the envelope of the deck. The historical road slab controls the thickness of the concrete submodel.

Parameter	Reference scale	Model scale
Main span L	853.44 m	8.5344 m
Aerodynamic width B	12.00 m	120.0 mm
Fence height H	2.40 m	24.0 mm
Edge plate thickness a	0.120 m	1.20 mm
Equivalent cross plate b	0.5313 m	5.313 mm
Historical road slab [1]	0.13335 m	Prototype local model

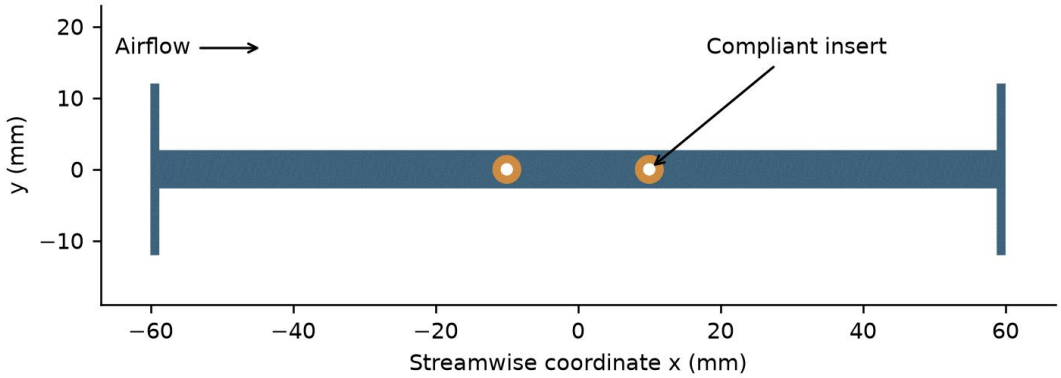

Figure 2. The generated cross-section at 1:100. Two bonded circular inserts carry the deck through fixed internal cores. Dimensions on the axes refer to the computational model.

The section is centred on the x–y origin. Wind travels along +x, y points upward and z follows the bridge. Positive rotation about +z lifts the downstream edge. Both idealized edge plates extend equally above and below the cross plate. Small through-deck features and rail porosity are omitted. Longitudinally discrete floor beams enter only the two-bay spatial model. The archived road-deck drawing [1] provides a separate check on later structural detailing.

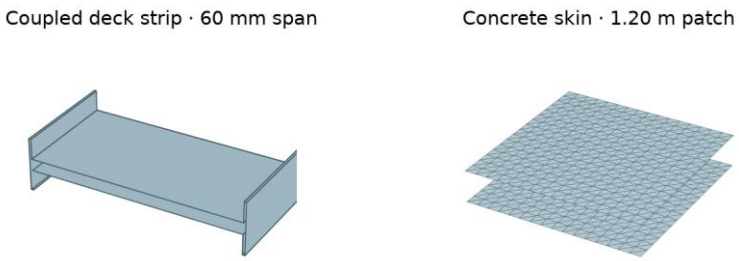

Figure 3. Left, the optional 60 mm prismatic strip. Right, the upper and lower skins of the prototype concrete patch. The patch receives its boundary history from the separate 304.8 mm two-bay segment in Figure 7. The panels use independent scales.

2.1 Two boundary value problems

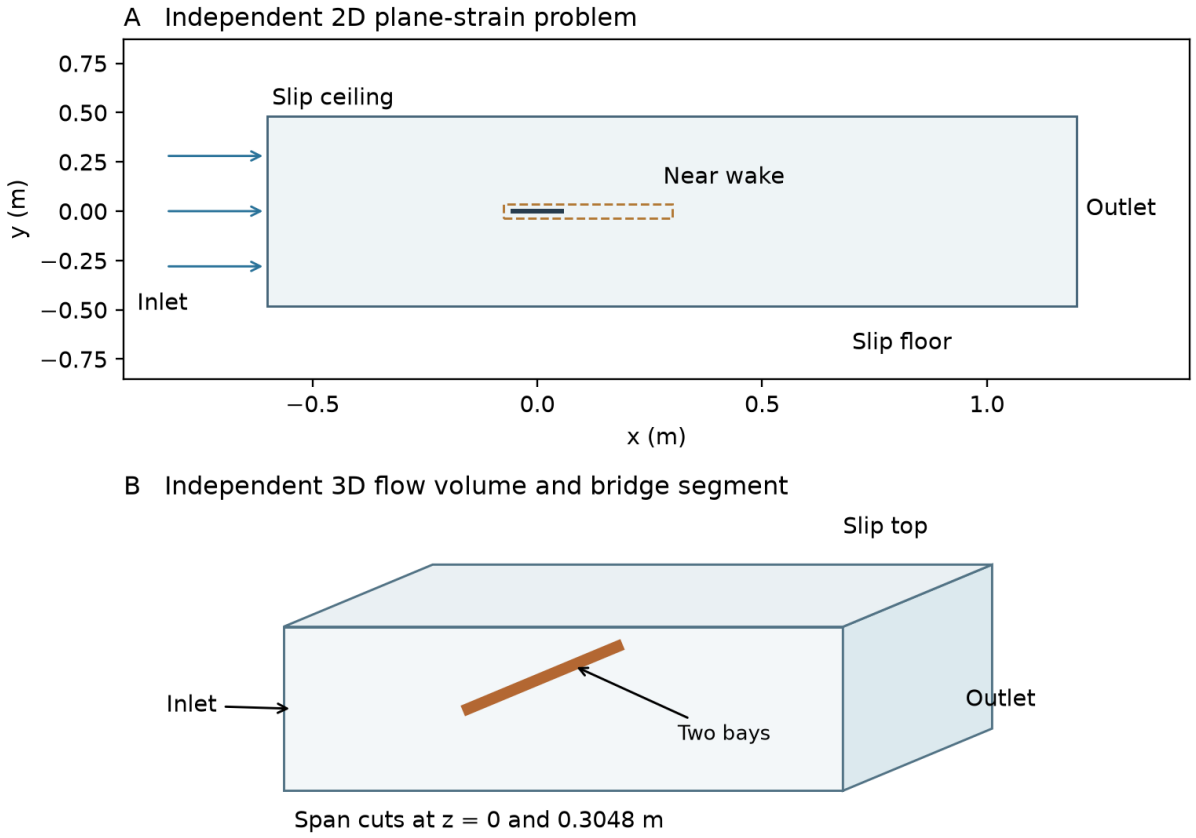

Figure 4. Fluid and structural problem definitions in model coordinates. The rectangular box around the planar section marks the initial near-wake refinement zone. The oblique view locates the two-bay solid within the 3D air domain.

The planar calculation assumes a prismatic system of infinite longitudinal extent, $\partial(\cdot)/\partial z = 0$. Its flow has two velocity components and its structure has two translation components. A closed 2D fluid domain surrounds a separately meshed 2D elastic body. The interface integral is a line integral and its resultant has units of N/m. This problem can resolve the phase between the local moving wall and the wake.

The spatial calculation has a finite 30.48 m prototype length and three translations per solid node. The two girders distribute loads through a slab, two transverse floor beams and four discrete attachment groups. Pressure and viscous traction act on the actual wetted faces. Out-of-plane strain, spanwise fluid transport, differential hanger reactions and warping are available observables. Sectional plots taken from this model are postprocessing views only.

The planar section and the two-bay model differ in geometry, support compliance and dimensionality. The package also contains a 60 mm prismatic strip with the planar H profile and compliant inserts. The campaign includes its mesh and boundary definitions only. The comparison of completed flow histories therefore cannot isolate the effect of dimensionality.

3 Scaling the numerical experiment

Let $\lambda = L_m/L_p = 0.01$. Subscripts m and p denote the model and prototype. Preserving the ratio of inertia to gravity, $U^2/(gL)$, at equal g gives $U_m/U_p = \sqrt{\lambda}$. From $t \approx L/U$, the time ratio is $\sqrt{\lambda}$ and the frequency ratio is $1/\sqrt{\lambda}$. These choices also preserve reduced velocity $U/(fB)$ when the structural frequencies meet their targets. Gravity enters the span through the specified equilibrium geometry and cable tension.

$$U_m = 0.1U_p, t_m = 0.1t_p, f_m = 10f_p \tag{1}$$

Equal fluid densities give a dynamic-pressure ratio λ. Matching inertia to aerodynamic pressure requires the same density ratio of structure to fluid. Thus line mass scales as λ^2, sectional mass moment of inertia as λ^4, force as λ^3 and total moment as λ^4. Matching elastic strain gives $E_m/E_p = \lambda$. For geometrically similar structural sections both EI and GJ scale as λ^5. Prestress expressed as an axial force scales as λ^3. Structural damping ratios are additional independent targets.

$$\mathrm{Re}_H = \frac{\rho UH}{\mu}, U_r = \frac{U}{f_\theta B}, \mathrm{St}_H = \frac{f_s H}{U} \tag{2}$$

With ordinary air at both scales the Reynolds-number ratio would be $\lambda^{3/2} = 0.001$. Exact Reynolds similarity requires $\mu_m = \lambda^{3/2}\,\mu_p$. Resolving the resulting thin shear layers would remove much of the saving sought here. The pilot instead uses the reduced-Re benchmark of [3]. At $U_m = 1.8$ m/s, $H_m = 0.024$ m and $\rho = 1.247$ kg/m^3, setting $\mu_m = 5.38704 \times 10^{-6}$ Pa s gives $\mathrm{Re}_H = 10{,}000$. This is an artificial working fluid. The reported event-scale value in [3] is 3.06×10^6.

Table 2. A dry natural frequency and an in-wind response frequency have different roles. Tuning the model to the observed in-wind motion would compromise the comparison.

Quantity	Prototype to model example	Use
Reference dynamic pressure	202.014 → 2.02014 Pa	Traction scale
Vertical response band	0.60–0.63 → 6.0–6.3 Hz	Historical response comparator
Dry torsion benchmark [3]	0.1875 → 1.875 Hz	Calibration comparator
Torsional response [3]	About 0.23 → 2.3 Hz	Historical response comparator

Dimension reduction, a short strip and a reduced Reynolds number control cost. A uniform change of dimensions at fixed dimensionless resolution alone would leave the number of cells and steps per oscillation essentially unchanged.

4 Air loads and the growth of an oscillation

For a moving mesh, let w be grid velocity and χ a fixed mesh coordinate. Applying momentum balance to a control volume with flux velocity u − w gives the arbitrary Lagrangian–Eulerian form below. For constant density and viscosity, incompressibility removes the volumetric part of the viscous stress. Pressure is measured relative to the outlet.

$$\nabla \cdot \mathbf{u} = 0, \rho \left[\frac{\partial \mathbf{u}}{\partial t} |_{\chi} + ((\mathbf{u} - \mathbf{w}) \cdot \nabla)\mathbf{u} \right] = \nabla \cdot \boldsymbol{\sigma}_f \tag{3}$$

$$\boldsymbol{\sigma}_f = -p\mathbf{I} + \mu \left[\nabla \mathbf{u} + (\nabla \mathbf{u})^{\mathrm{T}} \right], \mathbf{u}_{\Gamma} = \frac{\partial \mathbf{d}_{\Gamma}}{\partial t} \tag{4}$$

With n pointing out of the solid into the air, the fluid traction on the deck is $\tau = \boldsymbol{\sigma}_f$ n. Traction equilibrium sets σ_s n = τ. A force balance on the solid yields $\rho_s \partial^2 d/\partial t^2 = \nabla \cdot \sigma_s$ in the small-displacement pilot. The two zones exchange displacement and traction at every physical step. Integrating the work-conjugate components around one section gives

$$L' = \oint_{\Gamma} \tau_y \, ds, M' = \oint_{\Gamma} [(x - x_0)\tau_y - (y - y_0)\tau_x] \, ds \tag{5}$$

where (x_0, y_0) is the instantaneous section center. Lift and moment are per unit span. With $q\infty = \rho U^2/2$, use $C_L = L'/(q\infty B)$ and $C_M = M'/(q\infty B^2)$. To compare our values with [3], multiply our coefficients by B/H and $(B/H)^2$, respectively. Compare dimensional integrals first to detect axis or origin errors.

4.1 Diagnostic for flutter

For small heave h and pitch θ of a symmetric section write $q = [h, \theta]^T$, $F = [L', M']^T$. Linearizing about the dry equilibrium gives $M\ddot{q} + C\dot{q} + Kq = F$. Multiplication by $\dot{q}^T$ and integration over one cycle separates the change in stored energy from the work done by the fluid and the damping loss.

$$\Delta E = \int_{t_0}^{t_0+T} \left(L'\dot{h} + M'\dot{\theta} \right) dt - \int_{t_0}^{t_0+T} \dot{\mathbf{q}}^{\mathrm{T}} \mathbf{C}\dot{\mathbf{q}} \, dt \tag{6}$$

For harmonic pitch $\theta = A \sin \omega t$ and moment $M' = M_a \sin(\omega t + \varphi)$, pitch work over a period is $\pi A M_a \sin \varphi$. Equation (6) gives the change in kinetic plus elastic energy of the reduced system. Only a closed trajectory permits a closed-loop work integral. The recorded crossings need not close in amplitude or velocity. Positive pitch work measures energy supplied in one coordinate. Identification of flutter also requires a persistent growth rate, physical damping and consistent behavior under refinement.

4.2 Plane strain elasticity and interface work

Let d = (u, v, 0) be independent of z. The symmetric gradient gives $\varepsilon_{xx} = \partial u/\partial x$, $\varepsilon_{yy} = \partial v/\partial y$ and $\gamma_{xy} = \partial u/\partial y + \partial v/\partial x$. The constraints are $\varepsilon_{zz} = \gamma_{xz} = \gamma_{yz} = 0$. Substitution into the three-dimensional isotropic law $\sigma = 2G\varepsilon + \lambda_L \operatorname{tr}(\varepsilon) I$ gives

$$G = \frac{E}{2(1+\nu)}, \lambda_L = \frac{E\nu}{(1+\nu)(1-2\nu)} \tag{7}$$

$$\sigma_{xx} = (\lambda_L + 2G)\varepsilon_{xx} + \lambda_L \varepsilon_{yy}, \sigma_{xy} = G\gamma_{xy} \tag{8}$$

$$\sigma_{yy} = \lambda_L \varepsilon_{xx} + (\lambda_L + 2G)\varepsilon_{yy}, \sigma_{zz} = \lambda_L(\varepsilon_{xx} + \varepsilon_{yy}) \tag{9}$$

Consequently σ_{zz} generally survives even though ε_{zz} vanishes. Include it in the deviatoric tensor when reducing the 2D stress to a von Mises measure. A 3D free surface instead prescribes a traction, and permits strain in z. A dry patch with prescribed uniform ε_{xx} and zero other strains provides a constitutive check on the input setting before any wind calculation.

Multiplying solid momentum balance by an admissible virtual displacement, integrating the divergence term by parts, and retaining the interface term gives the weak form below. All integrals are over undeformed geometry for the small-motion pilot. For the planar case, A is the x–y section and Γ its wetted perimeter.

$$\int_A \rho_s \, \delta\mathbf{d} \cdot \ddot{\mathbf{d}} dA + \int_A \delta\boldsymbol{\varepsilon} : \boldsymbol{\sigma} dA = \int_\Gamma \delta\mathbf{d} \cdot \boldsymbol{\tau} ds \tag{10}$$

For 3D replace area by volume and line by surface. With a displacement map $d_f = P\, d_s$, the force returned to structural nodes must be $P^T f_f$ under the same sign convention for applied loads. Then $f_s \cdot \delta d_s = f_f \cdot \delta d_f$. This virtual-work identity checks pressure and shear transfer even on nonmatching meshes. During a coupled step monitor the traction imbalance, displacement change, iteration residual and minimum moving-cell volume.

A two-point section diagnostic gives heave from mean edge motion. For edge coordinates $(x_\pm, y_\pm)$ use $\theta = \operatorname{atan2}(y_+ - y_-, x_+ - x_-)$ relative to the reference orientation. Figure 12 uses a rigid fit over all deck nodes with reference tributary-area weights, equivalent to mass weights for the uniform deck material. Figure 16 uses a chord between two interpolated slab points at each station.

4.3 Separating a forced wake response from flutter

Billah and Scanlan [6] related the destructive torsional mode to motion-dependent aerodynamic damping. To test the alternative fixed-wake forcing mechanism, fix the bridge and measure the wake frequency $f_s(U)$. The reference Strouhal relation gives $f_s = St_H\ U/H$. For a linear heave oscillator forced at ω_s with lift amplitude L_0, balance inertia, damping and stiffness using $h = Re(\hat{h}\ exp(i\omega_s t))$. Taking the magnitude gives

$$|\hat{h}| = \frac{L_0/k_h}{\sqrt{\left(1-r^2\right)^2 + \left(2\zeta_h r\right)^2}}, r = \frac{\omega_s}{\omega_h} \tag{11}$$

For prescribed periodic forcing, finite damping bounds the resonant peak. A synchronization test requires wake and structural frequencies, phase and bandwidth over a range of wind speeds. The fixed-wake Strouhal estimate is a control. Once the deck moves, the circulation and instantaneous separation points can depend on its displacement and velocity.

For small motions fit the harmonic part of the sectional load to $F_a = K_a q + C_a \dot{q}$, allowing both matrices to depend on U and reduced frequency $k = \omega B/(2U)$. Separate harmonic heave and pitch identification tests, or independent coupled records with adequate excitation, are needed to identify the four complex transfer terms. For $q = v\ exp(st)$, a nonzero v requires

$$det[s^2\mathbf{M} + s(\mathbf{C} - \mathbf{C}_a) + (\mathbf{K} - \mathbf{K}_a)] = 0 \tag{12}$$

At neutral stability $Re(s) = 0$ and the oscillation frequency must be consistent with the k used to identify the aerodynamic terms. For torsion alone with moment a stiffness term proportional to θ and a damping term proportional to angular velocity, subtract the respective aerodynamic coefficients from the dry torsional stiffness and damping. A positive stiffness with negative effective damping gives growing oscillations. A vanishing effective stiffness has a different signature. Track both the growth rate and the measured signed cycle work in Eq. (6).

Dividing the heave balance by $\rho U^2 B$, setting $h = B\hat{H}$ and time $\tau = tU/B$, gives the following nondimensional equation. Primes here denote derivatives with respect to τ. The same substitution in pitch uses the moment scale $\rho U^2 B^2$.

$$m^*\left[\hat{H}'' + 2\zeta_h \kappa_h \hat{H}' + \kappa_h^2 \hat{H}\right] = \frac{C_L}{2} \tag{13}$$

$$I^*\left[\theta'' + 2\zeta_\theta \kappa_\theta \theta' + \kappa_\theta^2 \theta\right] = \frac{C_M}{2} \tag{14}$$

Here $m^* = m'/(\rho B^2)$, $I^* = I'/(\rho B^4)$ and $\kappa_j = 2\pi f_j B/U$. Matching geometry and wind speed alone leaves mass ratio, inertia ratio and the two damping ratios unconstrained. Dry frequencies and damping are independent inputs. Paired seed rotations and wind-off transients would help separate growth from startup response. The historical wind at failure and the model's linear onset speed are distinct comparison quantities.

5 Two dimensional plane strain model

The first coupled model represents a prismatic deck and two buried elastic supports in the x–y plane. The wind excites translations of the continuum nodes. Heave and pitch follow from the motion of the two girder edges. There is no prescribed rotational degree of freedom, harmonic force or initial twist. This arrangement makes it possible to measure the phase of the aerodynamic moment relative to rotation.

5.1 Constructing the planar regions

Twelve straight segments define the 120 × 24 mm envelope in Figure 2, including the 1.20 mm edge plates and the 5.313 mm cross plate. The support annuli are centred at x = ±10 mm, y = 0, with inner and outer radii of 0.9 and 2.0 mm. The deck excludes both outer disks. Each annulus bonds to the deck around an empty core. The annulus exterior shares the deck nodes. The inner rim supplies the fixture.

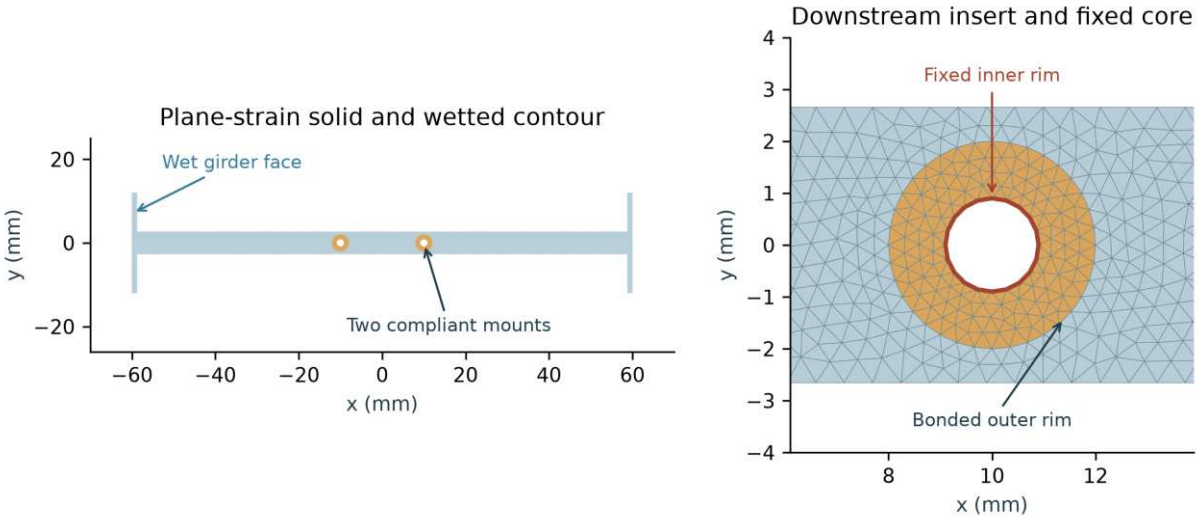

Figure 5. The two gold inserts transfer load to the fixed cores. The enlarged view at right uses the actual structural TRI3 mesh. Red marks the fully restrained inner boundary. The empty cores sit inside the structure and carry no air load.

A 1.80 × 0.96 m rectangle bounds the flow domain. The inlet lies five deck widths upstream of the section center and the outlet lies ten widths downstream. Subtracting the H profile leaves the air domain. Meshing the air, deck and insert regions together preserves common interface nodes before the zones are exported separately.

5.2 Constitutive and kinematic assumptions

Each structural TRI3 has linear shape functions and two translational unknowns per node. The displacement interpolation gives constant in-plane strain within each reference element. Plane strain enforces zero longitudinal strain, and the 3D isotropic stress law supplies the longitudinal stress in Eq. (9). The core rim restrains both in-plane components at 40 nodes along 40 edges. Neither the exterior plate edges nor the annulus–deck bond is independently fixed.

5.3 Planar discretization and mass assignment

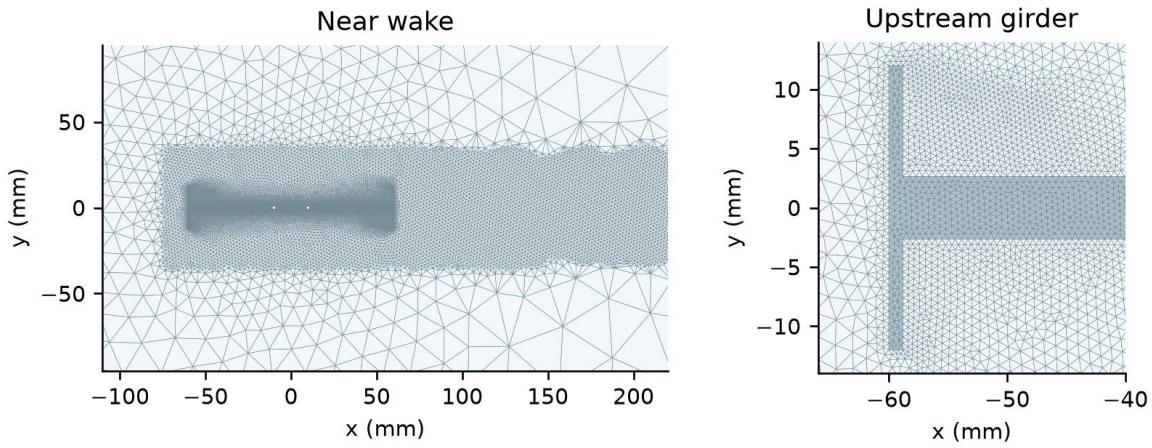

Figure 6. Triangular fluid mesh in the near wake and at the upstream girder. Both panels are in the x–y plane. Structural triangles inside the profile use a separate constitutive law.

Gmsh targets edge lengths of 0.55 mm along the section and 0.35 mm at the inserts. The wake box extends from x = −75 to 300 mm and y = −36 to 36 mm, with a 2 mm target. The size transitions over 60 mm toward an 85 mm outer target. The nominal discretization contains 25,420 fluid triangles, 5,636 deck triangles and 480 insert triangles. The assembled mesh has 15,821 nodes and 596 shared interface edges.

Table 3. Nominal planar mesh before calibration. The reported moving-section runs use an insert modulus of 97.44 Pa (Section 11). The effective deck density matches the prescribed line mass of the idealized section.

Domain	Material parameters	Discretization and purpose
Air	$\rho = 1.247$ kg/m³, $\mu = 5.38704$ µPa s	Incompressible Newtonian flow on triangular dual control volumes
Deck	$E = 2.10$ GPa, $\nu = 0.30$, $\rho = 1{,}092.08$ kg/m³	Plane-strain linear elasticity, equivalent deck mass
Inserts	$E = 300$ Pa, $\nu = 0.35$, $\rho = 100$ kg/m³	Bonded elastic annuli with fixed inner rims

Analytical area subtraction sets the target mass per unit span to 0.7198 kg/m. Direct integration over the polygonal mesh gives 0.719935 kg/m, a +0.019% difference. Integrating density times squared distance from the origin gives a polar mass moment per unit length of 0.00101038 kg m. This is 17.0% above the uniform-width approximation used for deck rotary inertia in the span model. Agreement in line mass alone therefore leaves a consequential torsional uncertainty.

5.4 Planar flow boundaries and coupling

The twelve inlet edges impose a velocity of (1.8, 0) m/s. The initial air field has that velocity and constant density. The twelve outlet edges impose zero gauge pressure. The upper and lower boundaries each have 22 slip edges. Normal flow vanishes there and the tangential velocity is free. The moving deck wall enforces viscous no slip and zero heat flux. With the energy equation disabled, zero heat flux serves as the SU2 viscous-wall marker. The fluid uses no turbulence closure in this reduced-Re pilot.

On each physical step the fluid solver updates gauge pressure and viscous traction at the current wall position. The structure receives the interface load. Its displacement is relaxed and passed back to the moving fluid grid. The fluid-zone grid deformation uses inverse-volume stiffness. Common reference nodes have different local numbers in the two exported files. Coordinate matching and opposed outward normals establish the interface correspondence.

Table 4. Nominal checkout settings. Sections 11.1, 11.2 and 11.4 report the overrides used for the plotted histories. Pseudo-time CFL controls inner convergence. Physical time and sampling are set by Δt and the write interval.

Setting	Value written in the planar deck	Physical or numerical role
Coupling and relaxation	Block Gauss–Seidel, up to 50 outer iterations, Aitken initial factor 0.5	Iterate displacement and load within each physical step
Fluid time integration	Second-order dual time stepping, implicit inner update, up to 60 iterations	FDS convective flux with MUSCL reconstruction, fixed pseudo-CFL 1000
Solid time integration	Implicit Newmark, β = 0.2601, γ = 0.52, up to 3 inner iterations	Small-displacement inertia and elastic restoring forces
Stopping and output	Residual log threshold −8, Δt = 50 μs, 2,000 steps, output every 10	0.10 s physical history with nominal 0.50 ms output spacing

The neutral model includes no material damping coefficient or independently measured damping ratio. Newmark integration introduces numerical dissipation. Section 11.8 quantifies the isolated modal integration loss. A still-air coupled decay test would also include damping from the fluid. At the 1.875 Hz model-scale torsional comparator, the original 0.10 s checkout spans less than one fifth of a cycle. Section 11 reports the extended calculations and the number of complete cycles observed.

6 Three dimensional two bay bridge segment

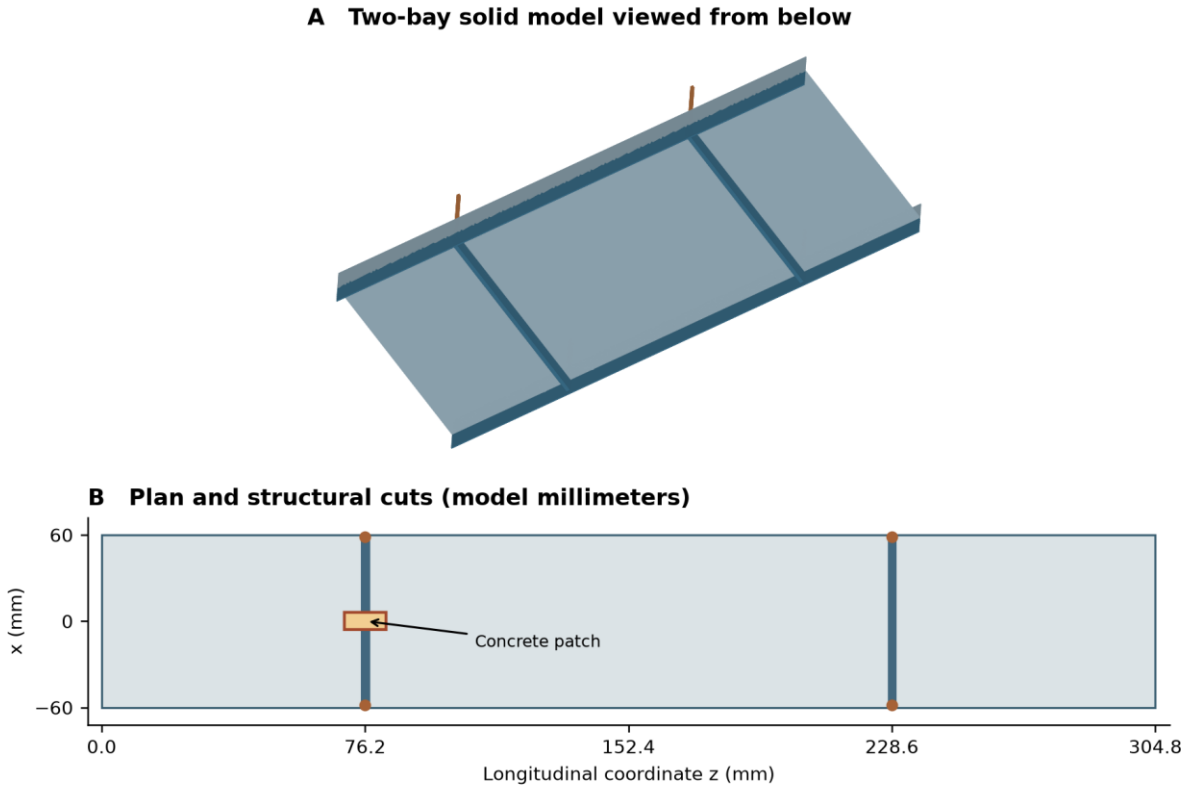

Figure 7. Underside view of the spatial model and plan showing the two transverse floor beams. The four attachment groups lie at their ends. Orange marks the local concrete patch in prototype registration.

At 1:100 scale, the 1.3335 mm thick slab extends 304.8 mm between the structural end cuts. Along its lateral edges, two plate girders are 24.384 mm deep and 0.47625 mm thick. The floor beams lie at z = 76.2 and 228.6 mm. Each spans the clear width and extends 9 mm below the slab soffit, with 2 mm thickness in z. Four 1.5 mm square suspender links join the slab at x = ±58.5 mm and terminate at y = 35 mm. Beam and suspender section sizes are pilot assumptions. The 152.4 mm station spacing corresponds to the historical 50 ft suspender interval [1].

The air block measures 1.80 × 0.96 × 0.3048 m. OpenCASCADE partitions its intersections with the segment. The source solid identifies each resulting volume as air, slab or steel. Internal slab–steel faces share nodes, so the structural interface is perfectly bonded. No contact law, reinforcement, joint slip or initial cable tension is assigned to this local continuum. The 3D case has its own material volumes, constraints and unstructured mesh.

6.1 Spatial supports and applied tractions

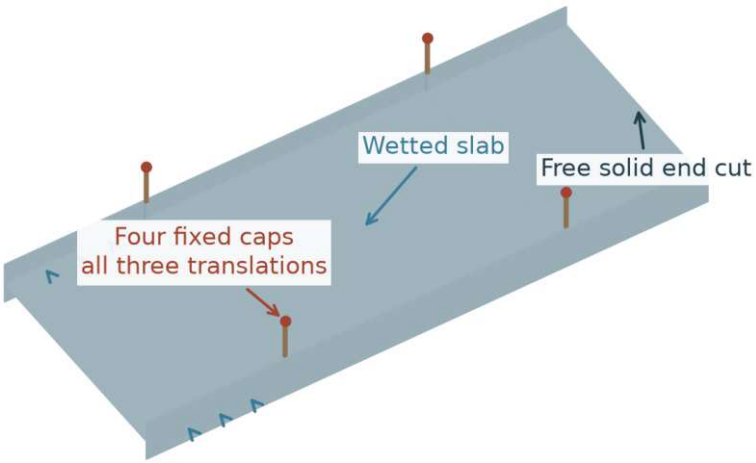

Figure 8. Blue arrows locate an exposed girder surface on which air traction acts. Red points locate the four fixed cap faces. The two structural cuts normal to z carry natural zero traction in the isolated segment.

Each cap restrains all three translations. Together the caps contain 20 restrained nodes and 16 boundary triangles. There are no nodal rotation constraints in a displacement-based TET4. The short elastic links provide support flexibility below the caps. The solid end cuts at z = 0 and 304.8 mm permit warping and local rotation but transmit no actions from the adjoining bays in this pilot. Section 7.1 derives the dynamic end impedance required for the span-compatible alternative.

Table 5. The cap surface is counted once per zone. On the solid it belongs to fix_all. On the air side it belongs to cap_wall. Fixed cap tractions can be integrated separately when closing the overall force balance.

Boundary	Structural condition	Fluid condition
Wetted deck, girders, beams and link sides	Pressure plus viscous traction; displacement returned to grid	Moving, viscous no-slip wall
Four cap surfaces	Three translations fixed	Stationary no-slip cap_wall marker
Front and back end planes	Free structural cuts	Slip, zero normal flow
Upstream and downstream faces	Air only	Velocity inlet along +x; outlet gauge pressure 0 Pa
Upper and lower air faces	Air only	Slip and symmetry for moving-grid deformation

The two-bay air domain has the same inlet speed, density and viscosity as the independent planar model. The front and back slip planes limit admissible spanwise flow at the ends. Check both the end treatment and the retained segment length before interpreting spanwise coherence. A difference in measured frequency between the planar and spatial cases can also arise from support compliance or rotary inertia.

6.2 Spatial mesh and constitutive assignment

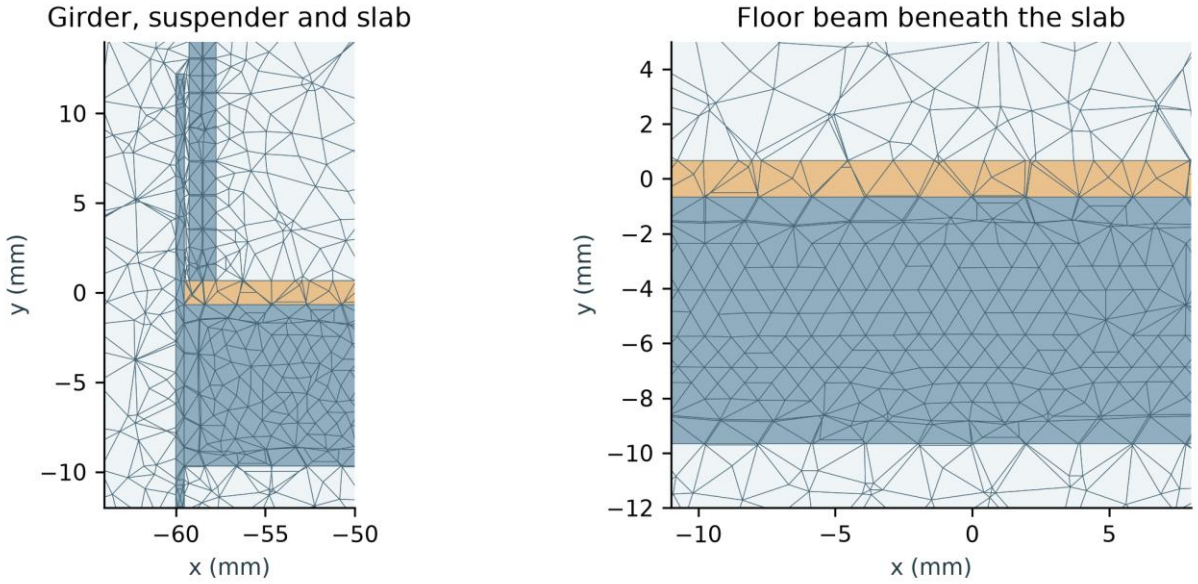

Figure 9. Intersections of the actual three-dimensional tetrahedra with the plane z = 76.23 mm, just inside the first floor beam. Blue denotes steel and ochre denotes concrete. The polygons show the section through TET4 elements; the neighboring pale region belongs to the air mesh.

Netgen optimizes element quality after generation of the conforming tetrahedral mesh. The resulting mesh contains 40,469 steel and 68,230 slab elements. A distance field controls size near wetted surfaces. At the fine grade, the nominal minimum size is 1.976 mm and the outer target is 36.4 mm, blended over 2–130 mm from the wetted surface. A wake box adds a 6.24 mm target between x = −80 and 270 mm and y = ±45 mm. Intersections of CAD faces force smaller edges near thin members. A target size alone does not establish a number of elements across a plate thickness.

Table 6. Structural materials use scaled stiffness and the unscaled density ratio. The spatial geometry explicitly represents a thin slab, whereas the planar aerodynamic cross plate has equivalent thickness.

Property	Slab continuum	Steel continuum
Young modulus and Poisson ratio	0.30 GPa, 0.20	2.10 GPa, 0.30
Density	2,400 kg/m³	7,850 kg/m³
Members	Road slab	Girders, floor beams and suspender groups
Interface and response	Bonded TET4, three translations per node	Bonded TET4, three translations per node

In each constant-strain structural tetrahedron the three displacement components determine six independent stress components. The fluid is cell-vertex finite volume on the tetrahedral mesh, with three velocity components and pressure. No beam, shell, hinge or truss element enters this coupled deck. Verify bending compliance against a shell or layered-solid reference before using through-thickness stresses for damage assessment.

6.3 Spatial coupling and independent input checks

The unmodified three-dimensional master deck uses the same 50-iteration partitioned coupling loop, Aitken initialization, physical time step and output interval as Table 4. At each step all three components of the structural interface displacement update the air grid. The return load includes pressure and viscous traction on moving wetted faces. Four fixed caps use a separate stationary air-wall marker. The spatial solid uses the full 3D elastic tensor and implicit Newmark integration.

Table 7. Counts come from the exported SU2 zone files and preflight reports. The same 16 cap triangles are excluded from each moving-interface count.

Model	Air cells	Solid cells	Moving interface
Coarse two-bay	92,325	33,818	18,778
Medium two-bay	218,923	59,701	34,710
Fine two-bay	532,244	108,699	65,279

An independent reader checked positive signed element measures, unique coordinates within each zone, the exported per-element material indices and support node sets. Every fluid interface triangle had a solid counterpart at the same coordinates and with the opposite normal. No physical face was assigned two boundary markers within either zone. The full audit is supplied in mesh_audit.json.

A regular simplex has mean-ratio quality Q = 1. For tetrahedra use $Q = 12(3V)^{2/3}/\Sigma\ell^2$, where the sum covers the six edge lengths. In the fine deck, median Q is 0.885 for fluid, 0.897 for slab and 0.579 for steel. The minimum steel value increased from 0.0266 in the previous fine mesh to 0.251 after remeshing and quality optimization. Slender elements in the thin steel members make cut resultants and bending-compliance refinement tests more informative than a single maximum stress.

The volume integral of structural density gives 0.207769 kg for the isolated bridge segment, or 0.681657 kg/m. The planar mass target is 0.7198 kg/m. These values represent different idealizations and the discrepancy must be retained in dry-mode comparisons. The optional 60 mm uniform strip in models/3D supplies the dimensionality control for the planar H geometry; it has no discrete floor beams.

7 From section forces to span motion

The span model resolves a feature that a short strip cannot represent. Two main-span halves can twist in opposite directions while midspan records almost no rotation. The reduced structure contains 56 equal bays, two cable axes and 55 interior stations. At each interior station the degrees of freedom are deck heave h and twist θ. End heave and twist vanish. Free end slopes give the bending model simple supports. Rigid transverse sections tie the cable increments to $e\pm = h \pm B\theta/2$. Slack hangers and tower motion require a subsequent nonlinear model.

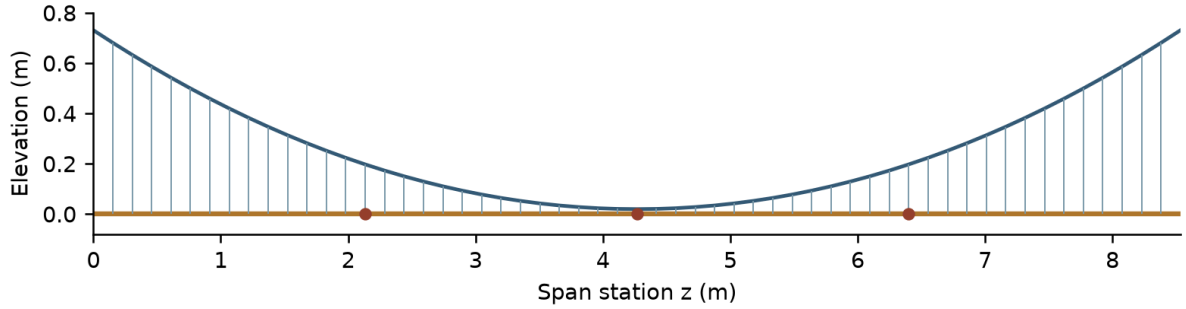

Figure 10. Main-span elevation at model scale. Both cable axes coincide in elevation. Quarter-span and midspan probes resolve the expected sign change. The vertical scale is enlarged.

For bay length d, cable slope s' and $\xi = \sqrt{(1 + s'^2)}$, a vertical end-displacement difference Δe changes cable length by $(s'/\xi)\Delta e$ to first order. Expansion of length to second order gives geometric stiffness $H_0/(d\xi^2)$ per bay for horizontal tension H_0. The axial stiffness EA/Lc acts on the sum of the first-order length changes. With D the station difference operator and $v = D^T(s'/\xi)$, the tangent of one cable is

$$\mathbf{K}_c = \mathbf{D}^{\mathrm{T}} diag\left(\frac{H_0}{d\xi^2}\right)\mathbf{D} + \frac{EA}{L_c}\mathbf{v}\mathbf{v}^{\mathrm{T}} \tag{15}$$

The two cables add $2Kc$ in heave and $2(B/2)^2Kc$ in twist. Deck curvature and twist gradients add $EI\, d\, D_2{}^T D_2$ and $(GJ/d)D^TD$, where D_2 is the second difference divided by d^2. Lumped inertia includes the true segment lengths of both cables and deck rotary inertia $m'B^2/12$. The resulting 110 × 110 mass and tangent matrices accompany the model [1, 3].

The sag is L/12. Scaled horizontal tension per cable is 58.3 N, deck EI is 3.15 N m^2 and GJ is 5.2164×10^{-5} N m^2 [3, Table 2]. Dead-load equilibrium is assumed about the supplied parabola. The archived eigenfrequencies characterize this assumed equilibrium. Interpolate station motion to each aerodynamic strip with H_s. Virtual work requires the return map $F = \Sigma\, H_s{}^T\, [L', M']^T\, \Delta z$. A live span-to-flow driver is still required. A single replicated strip history would impose perfect coherence and could suppress an antisymmetric mode.

7.1 Three dimensional section forces and boundary reduction

For a cut at constant z define traction t = σ$\mathbf{e}_z$. Taking moments about the chosen section axis with r = (x − x_0, y − y_0, 0), the six section resultants are the integral of t and the integral of r × t over the material in the cut. The torsional moment is

$$T_z = \int_A \left[(x - x_0)\sigma_{yz} - (y - y_0)\sigma_{xz}\right] dA \tag{16}$$

For Figure 22 the integration uses the undeformed cuts and the fixed axis x_0 = y_0 = 0, consistent with the small-strain segment. The shear force in y is $\int\sigma_{yz}$ dA, the axial force is $\int\sigma_{zz}$ dA, and the bending moment about x is $\int(y - y_0)\sigma_{zz}$ dA. Evaluate them at both sides of each floor beam. Differences across a small bay should balance integrated aerodynamic loads, attachment reactions and the rate of change of linear and angular momentum. Integrate element stresses at the cut and compare with independent nodal reactions. A peak stress near an idealized clamp is mesh-sensitive.

Partition the span's linearized equilibrium into retained cut degrees of freedom b and interior coordinates i. For a harmonic motion of frequency ω, Z = K + iωC − ω^2M. Eliminating interior displacements by block substitution gives the effective end impedance and load.

$$\mathbf{Z}_r = \mathbf{Z}_{bb} - \mathbf{Z}_{bi}\mathbf{Z}_{ii}^{-1}\mathbf{Z}_{ib}, \mathbf{F}_r = \mathbf{F}_b - \mathbf{Z}_{bi}\mathbf{Z}_{ii}^{-1}\mathbf{F}_i \tag{17}$$

A free-end segment implicitly sets this surrounding impedance to zero. Clamping a cut would impose the opposite limiting condition. Compare the condensed impedance or imposed global cut motion over the frequency range containing the heave and pitch modes. Near a pole of $\mathbf{Z}_{ii}$ retain the relevant interior mode explicitly. For time-domain replay preserve causality by retaining those modes or by using a fitted dynamic boundary.

At each 3D section fit translation and rotation to the actual displacement of several deck nodes. The difference between the full displacement and this rigid fit measures warping and local bending. The two-degree-of-freedom span model cannot supply axial strain or detailed slab warping on its own. Resolve those fields in the spatial segment using compatible boundary motion, then transfer them to the concrete patch. This step is essential to interpreting damage induced by a globally twisting deck.

8 Transfer of segment histories to the concrete patch

The spatial donor is the isolated two-bay model near the prototype quarter span. Its saved fields provide synchronized displacement, pressure and wall shear. At slab–beam contact, the adjacent steel element supplies traction. The suspended-span calculation has a separate prescribed sectional load history and contributes no displacement to the patch. This distinction limits the replay to loads and strains generated by the locally supported segment.

Convert the time and traction histories back to prototype units. With the scales in Section 3, $t_p = 10t_m$, $u_p = 100u_m$ for structural displacement, $\tau_p = 100\tau_m$, $F_p = 10^6 F_m$ and total moment scales back by 10^8. A 2D line force instead scales back by 10^4. Interpolate pressure and shear to the actual slab skin and integrate over overlap areas. For target shape functions N_i, the consistent nodal forces are

$$\mathbf{f}_i = \int_A N_i \boldsymbol{\tau}_p dA, \sum_i \mathbf{f}_i = \int_A \boldsymbol{\tau}_p \, dA, \sum_i \mathbf{r}_i \times \mathbf{f}_i = \int_A \mathbf{r} \times \boldsymbol{\tau}_p dA \tag{18}$$

The registered segment displacement prescribes motion on the patch perimeter. A rigid fit on that perimeter removes translation and rotation. Tractions are rotated to the same frame before assembly. The remaining deformation drives the small-strain patch. The initial patch state is unstressed and undamaged, so earlier service loads and pre-existing cracking are outside the history.

8.1 Concrete and steel

The concrete patch occupies 1.20 × 1.20 m at the prototype quarter span and spans the 0.13335 m slab thickness. Four elements through depth give 6,144 tetrahedra altogether. Prescribe the perimeter cut history, then apply consistent surface nodal forces on the free skin. Record the share carried as reactions at prescribed edge nodes separately in the work audit. Reinforcement, bond, joints and steel–concrete interaction need detail before extending a plain-concrete result to roadway failure.

For a scalar tensile damage variable D, $\sigma = (1 - D)\, C_0\, \varepsilon$. With elastic stress reaching f_t, $\varepsilon_0 = f_t/E$. Let w be localized opening and ℓ the element characteristic length. Using $w \approx \ell \varepsilon_{in}$ and integrating the softening traction gives $G_f = \int \sigma(w)\, dw$. This energy per area is held fixed under mesh refinement. The OOFEM idm1 trial card uses E = 30 GPa, ν = 0.20, f_t = 3 MPa and G_f = 100 J/m^2. These values illustrate the transfer and require independent material evidence. D measures continuum stiffness loss.

The transfer utility fits the rigid motion on the cut perimeter, rotates displacements and tractions into that frame and integrates each face traction to its three nodes. A manufactured rigid rotation with reversing traction gave zero residual cut displacement to the mapping tolerance. Across the three prescribed frames the maximum resultant errors were 1.78×10^{-12} N in force and 7.30×10^{-12} N m in moment. The check exercises the mapping only. For the fine two-bay mesh, a registered transfer map locates all 1,445 patch nodes by tetrahedral interpolation. It partitions the two slab skins into 2,702 overlap polygons. Where the slab contacts a floor beam, use the beam-to-slab traction in place of air pressure. The overlap centroid integrates the linear target shape functions exactly for facewise constant traction. Changes of source geometry require rebuilding the map.

The separate one-bay steel web file defines unloaded geometry and end sets. The coupled segment supplies elastic steel stresses only. A calibrated yield curve would be needed to use the equivalent stress $\sigma_{eq} = \sqrt{(3s:s/2)}$ to assess first yield, with s the deviatoric stress. The available constitutive laws supply neither plastic-strain histories nor rivet fracture.

9 Verification before historical interpretation

The TENSORA preprocessor found both domains, all supports and paired interface facets with zero unassigned fluid faces in each coupled deck. The planar structural deck explicitly selects PLANE_STRAIN. All three two-bay meshes include both slab and steel material zones. All signed simplex measures were checked during generation and oriented positively. These checks establish file consistency. They do not quantify error in shedding frequency, damping or damage.

Table 8. Accuracy targets for interpreting the results. Near zero, normalize work and moment errors by cycle peak magnitudes. Report unresolved discrepancies even when a case passes a numerical tolerance.

Test	Proposed comparison	Acceptance for interpretation
Dry structure	Independently documented modal frequencies and shapes	Frequency within 5%, modal assurance >0.95 for matched shapes
Fixed wake	$\mathrm{St}_H \approx 0.111$ in the 3D study [3], mean drag and RMS lift	Three-grid and two-step-size study, changes <3% in St and <5% in loads
Coupled section	Positive and negative work around the transition	Same growth sign after refinement, onset shift <5%
Full span	Opposite quarter-span twists and near-zero midspan	Compare phase, amplitude envelope and node locations
Damage replay	Resultants, moments and interface work	Normalized errors <1%, onset load and dissipated energy change <5% on refinement

The fixed-section grid sequence includes 11,630, 25,420 and 54,528 fluid triangles at grades 1.4, 1.0 and 0.7. The G200 half-step control isolates time discretization on the coarsest grid. The spatial comparisons change fluid and structural discretizations together. The four spatial donor grids share one prototype patch mesh, so the stress comparison tests sensitivity to donor fields. It does not test localization or crack-band convergence in the patch itself.

Song et al. [3] bracketed onset using suspended-deck responses at 8 and 9 m/s. Szabó et al. [4] independently interpolated the total damping of the original-deck configuration to zero at 9.0 m/s. These studies motivate the present model speeds of 0.8 and 0.9 m/s. Because the sweep changes both reduced speed and Reynolds number at fixed viscosity (Table 12), it does not isolate either effect. Section 12.3 evaluates the published thresholds against physical model evidence.

The comparisons in Table 8 are interpretation criteria. A small transfer residual establishes that the chosen map preserves a load or its work to the stated tolerance. Agreement with historical observations would additionally require independent evidence for the input wind, structural damping, support stiffness and the motion being compared. Section 12 evaluates the criteria against the archived results.

10 Model and data availability

The archive contains generators for the fixed section, moving sections, two-bay segment, optional uniform strip and span matrices. The principal 3D domain covers two suspender bays. The suspended-span matrices and prototype damage patch are separate models. Section 11 reports the calculations and the transfer of three-dimensional motion and traction to a damage patch. The span still requires motion-dependent aerodynamic loads, measured damping and independently identified material and connection properties for event reconstruction.

Table 9. Paths are relative to models. The neutral JSON is a backend payload. Meshes can be examined independently of the application. Applied segment and patch histories are in results/spatial. Material data use a trial calibration.

Package path	Contents and use
fixed2D /	Fixed-wall SU2 unsteady control using the coupled fluid mesh
2D / and bridge_segment /	Independent plane-strain and two-bay cases with split SU2 inputs
3D /	Uniform strip control for the dimensional comparison
assembly /	Complete three-span engineering context in VTK
span /	Reference axes in VTK, M and K in NPZ, interior h then θ ordering
damage /	Prototype TET4 geometry, cut and skin node sets, trial card, CSV schema
panel /	Prototype girder web geometry and cut sets for stress recovery

The run catalogue identifies completed runs, rejected trials and exact overrides. Section histories and cycle work are in results/section and results/section_cycle_work.csv. The three-dimensional aerodynamic force and moment, four support reaction histories, material damage trace and peak stress field are in results/spatial. The full-span prescribed-load check, paired spatial meshes and structural inertia comparisons are in results/qa. Raw solver restarts are retained separately at the archive location in README.txt. The movies in results/visualizations use native time-indexed fields.

10.1 Records underlying the reported comparisons

Each FSI time label is the SU2 physical iteration index multiplied by its configured time step. The zero label includes the first implicit flow update. During the 60 ms startup ramp the structural load is multiplied by the ramp fraction. Thus a nonzero fluid pressure at time zero is compatible with zero applied structural load. Times in the patch response are prototype seconds.

Fixed wake and moving section. Table 11 uses results/wake_metrics.csv. The step and grid differences come from results/qa/refinement.json. Table 12 uses results/speed_sweep/comparison.csv. Individual crossing intervals for the linear G200 case are in results/section_cycle_work.csv. The finite-strain G140 intervals, including the two with negative work, are in results/qa/NH-G140-pitch_cycles.csv. The admissible time windows and signed area checks are recorded in results/qa/support_study.json.

Suspended span and isolated segment. The uniform-load projection and damping checks in Figure 20 use results/qa/span/sensitivity.json. Matched local modes are in results/intermesh_modes.csv. Figure 22 uses the bands, cuts and balance files in results/spatial/torque. Figure 28 uses results/spatial/deck_fields/moment_parity.csv. Its reflection plane is the segment midpoint for the local load and the main-span midpoint for the global mode.

Concrete and roadway. Figure 17 uses results/spatial/damage_trace.csv. It records element maxima per increment. Figure 27 restricts the search to cells touching the upper skin. The plate_frames.csv ledger in results/spatial/torque identifies the native frame and scale of each annotation. Table 15 and Figure 33 use matched_velocity_probes.csv and frame_summary.csv in results/spatial/deck_fields.

Run status and exclusions. The catalogue in results/run_catalog.csv identifies discarded fixed-body runs with spurious negative drag and early coupled runs with incorrect material assignment. The completed linear G140 section remains admissible only through 0.950 model s. Its first saved solid inversion occurs at 0.960 s. The finite-strain G140 case is a separate run. The principal spatial time history is segment-series. The refined spatial histories end during the ramp.

11 Numerical results and verification

We first solved the generalized eigenproblem on the unstressed continuum sections and on the suspended-span tangent about its assumed prestressed equilibrium. The continuum matrices use the linear isotropic law, the original facets and clamps, and consistent element mass. The reduced span retains 55 interior stations for each displacement component. The frequencies below are in hertz at model scale. The corresponding prototype frequencies are one tenth of these values under the stated similarity law.

Table 10. Independent dry frequencies. The rotary and heave participation fractions use the mass inner product with uniform section rotation and vertical translation, respectively.

Calculation	Model frequency	Interpretation
Suspended span, first torsion	1.8694 Hz	Opposite signs at the quarter spans
Plane strain, initial mount	3.2803 Hz	99.996% of rotary participation
Plane strain, G200 trial mount	1.9057 Hz	Heave-dominated mode at 7.1173 Hz
Isolated two-bay segment, coarse mesh	20.84 Hz	Lowest mode has little heave or rotary participation

The span calculation puts the two quarter spans in opposite torsional phase. Its first torsional frequency differs by 0.30% from the 1.875 Hz dry comparator. The plane-strain section initially twists 75% faster than the span. We therefore reduced the trial mount modulus from 300 to 97.44 Pa using the squared target-to-initial frequency ratio. A separate eigensolution of the G200 mesh then gave 1.9057 Hz, 1.94% above the computed span target. This one-parameter fit leaves heave stiffness, rotary inertia and physical damping as independent uncertainties.

The in-house TENSORA v1.2.7 platform [5] generated the coupled model and solver decks. SU2 8.6.0 advanced the fluid and structural fields. OOFEM 3.0 integrated the separate concrete damage history. SU2 appends the structural zone number to the element-property filename. We supplied element_properties_1.dat and a zero thermal expansion coefficient for each material. We rejected runs whose logs reported a fallback to uniform material properties. The mesh and material files in the package reproduce the corrected assignment.

11.1 Wake of the fixed plane section

The fixed section used a no-slip deck, constant density and viscosity, and a 1.8 m/s crosswind. The following comparisons use second-order dual time stepping, limited MUSCL reconstruction, pseudo-CFL 65 and up to 45 inner updates. G200, G140, G100 and G070 designate planar mesh-size factors 2.0, 1.4, 1.0 and 0.7. The postprocessor uses the depth H = 24 mm for drag and Strouhal number and the width B = 120 mm for lift. Each coefficient refers to one metre of model span.

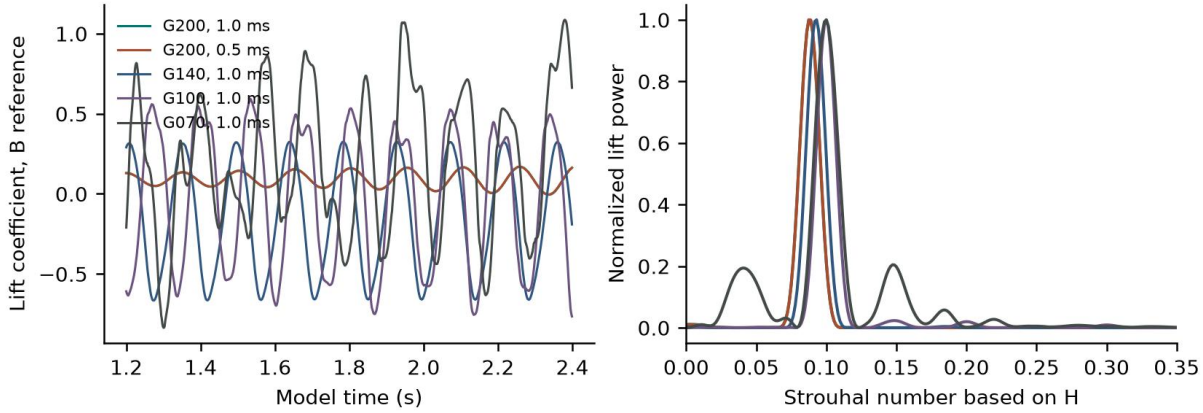

Figure 11. Lift over the common comparison window and its power spectrum. The spectrum uses a Hann window, linear detrending and eightfold zero padding. The bin spacing before zero padding equals the inverse window duration.

Table 11. Common analysis bounds are 1.1995–2.399 s in model time. Steps are 1 ms except for the 0.5 ms G200 control. The common frequency resolution is approximately 0.83 Hz. The RMS lift removes the window mean.

Case and step	Peak frequency and St	Mean drag and RMS lift
G200	6.56 Hz, 0.088	1.114, 0.047
G200 half step	6.56 Hz, 0.088	1.114, 0.046
G140	6.98 Hz, 0.093	1.586, 0.345
G100	7.50 Hz, 0.100	1.689, 0.428
G070	7.50 Hz, 0.100	1.773, 0.451

The time-step comparison changes peak Strouhal number by 0.0%, mean drag by 0.024% and RMS lift by 1.3%, relative to the half-step run. Grid comparisons below use the finer grid as denominator. The G200 to G140 comparison changes peak Strouhal number by 6.0%, mean drag by 29.8% and RMS lift by 86.4%. The G140 to G100 comparison changes peak Strouhal number by 6.9%, mean drag by 6.1% and RMS lift by 19.5%. The G100 to G070 comparison changes peak Strouhal number by 0.0%, mean drag by 4.8% and RMS lift by 5.1%. At least one comparison exceeds the prespecified frequency or load tolerance in Table 8. A reference three-dimensional wake calculation gave St ≈ 0.111 [3]. The present section, finite window and spanwise constraints differ from that study. The CSV also records first- and second-half peaks and upward crossing counts. On G070 the half-window peaks are 6.04 and 7.50 Hz. The common 7.50 Hz peak on the two finest grids therefore has limited spectral precision.

11.2 Two-way plane-strain response

The G200 model contains 6,608 fluid triangles and 1,648 structural triangles. The two systems exchange loads and motion on 302 matching edges. We used the 97.44 Pa insert, a 2.0 ms physical step and a linear 60 ms ramp of the load returned to the structure. After the ramp all pressure and viscous loads were applied. Each plotted motion point represents a mass-weighted rigid fit to the deck region of the independent planar continuum.

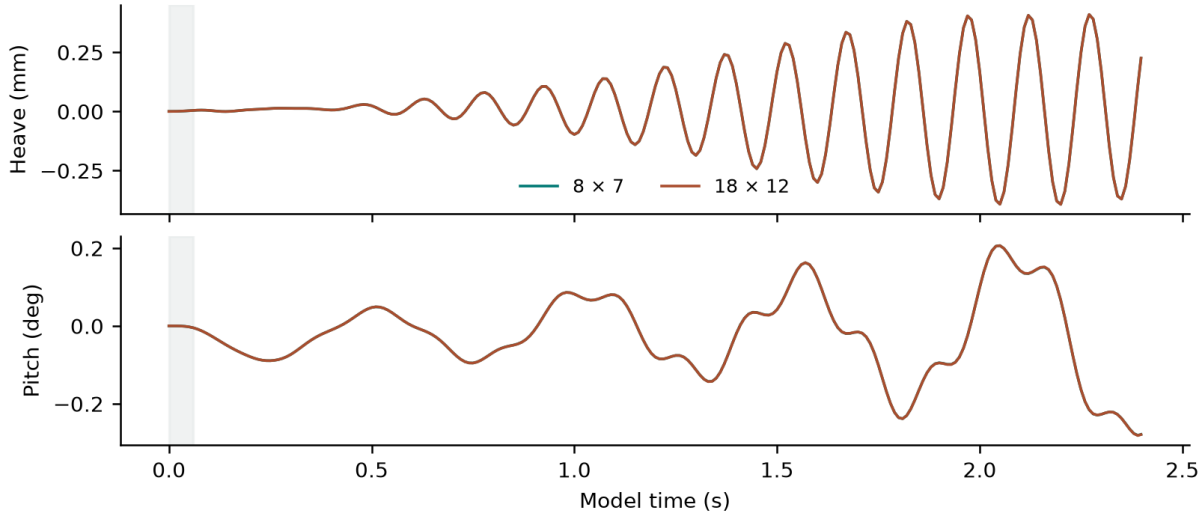

Figure 12. Heave of the deck centre and positive counterclockwise pitch. The legend gives the maximum outer and fluid inner iterations. The shaded interval marks the artificial startup ramp.

The 8 × 7 run (pseudo-CFL 60) covers 2.398 s of model time. Over this record, maximum absolute heave is 0.4094 mm and maximum absolute pitch is 0.2813°. The 18 × 12 run (pseudo-CFL 120) provides an iteration-sensitivity comparison to 2.398 s. Relative L2 differences over the common displacement frames are 0.07% in heave and 0.21% in pitch, using the latter run as the denominator. Its final mean log10 air inter-sweep residual was −5.91 against a nominal −8. Similar deck motion at the two iteration limits therefore tests sensitivity of those observables only.

The force history is sampled every 2 ms. Projected work uses the mean applied load at consecutive saved displacement frames and their displacement increment (nominal spacing 10 ms). We refer moment to the moving deck centre and integrate the applied lift and moment against heave and pitch increments. The cycle ledger retains 3 complete intervals between successive upward crossings after the ramp, using mean pitch as the crossing level. The crossing frequencies range from 1.75 to 1.97 Hz. Signed pitch work ranges from +0.14 to +0.99 μJ per metre of model span. All three intervals have positive projected pitch work. This projection excludes elastic distortion of the section and work associated with surge and heave. A short, damped or growing transient can contain both dry motion and wake forcing. The available record and damping calibration do not establish a flutter threshold.

11.3 Airflow around the moving plane section

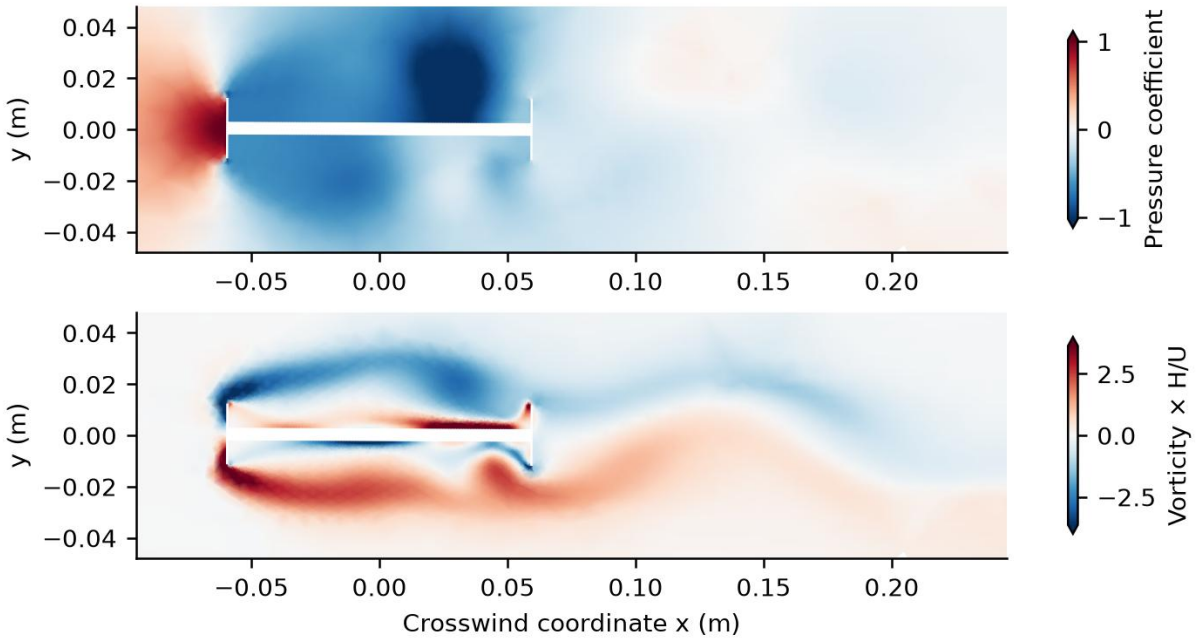

Figure 13. Gauge pressure and signed spanwise vorticity in the moving plane-strain calculation at 2.398 s model time. The shapes follow the native ALE grid. Colour limits clip the tails to resolve the shear layers.

The plotted triangles come directly from the fluid zone. The white deck region contains structural elements. Vorticity uses the 24 mm reference depth and the inlet speed. The pressure coefficient divides gauge pressure by 2.02014 Pa. The separation at the girder edges and the downstream wake can be located independently of a force-spectrum peak. At the fixed air probe x = 120 mm, y = 6 mm, the peak in vertical velocity is 6.56 Hz in the latter half of the history ending at 2.398 model s (100 Hz resampling). The corresponding lift and pitch peaks are 6.56 and 1.88 Hz. Their unpadded frequency resolution is approximately 0.83 Hz. These peaks sample the moving-deck wake.

The independently meshed G140 section contains 11,630 fluid and 3,254 solid triangles. The same support and fluid properties give a dry pitch frequency of 1.876 Hz. Before the first recorded solid-element inversion, the common post-ramp interval ends at 0.950 s. Normalized by G140 on that interval, the G200-to-G140 differences are 101.6% in heave and 84.2% in pitch. Section 11.12 examines the support deformation.

The companion plane-strain movie follows the computed vorticity field with a synchronized pitch trace. A signed aerodynamic work estimate requires load phase as well as motion amplitude. The force CSV retains both in-plane Cartesian components and the fixed-origin moment. The work ledger includes surge separately because the compliant inserts allow horizontal motion. An event-level inference would also require dry decay, positive and negative perturbations, and consistent growth and work under speed and mesh refinement.

11.4 Three-dimensional bridge segment

For the time-history pilot we independently meshed the complete two-bay geometry with 10,614 fluid and 6,805 structural tetrahedra. The 3,194 moving interface triangles exclude 16 fixed cap triangles. The slab, both edge girders, both floor beams and four attachments remain distinct geometric parts. To make the recording affordable, this mesh is coarser than the three resolution meshes in Table 7. It provides a test of transfer and structural equilibrium.

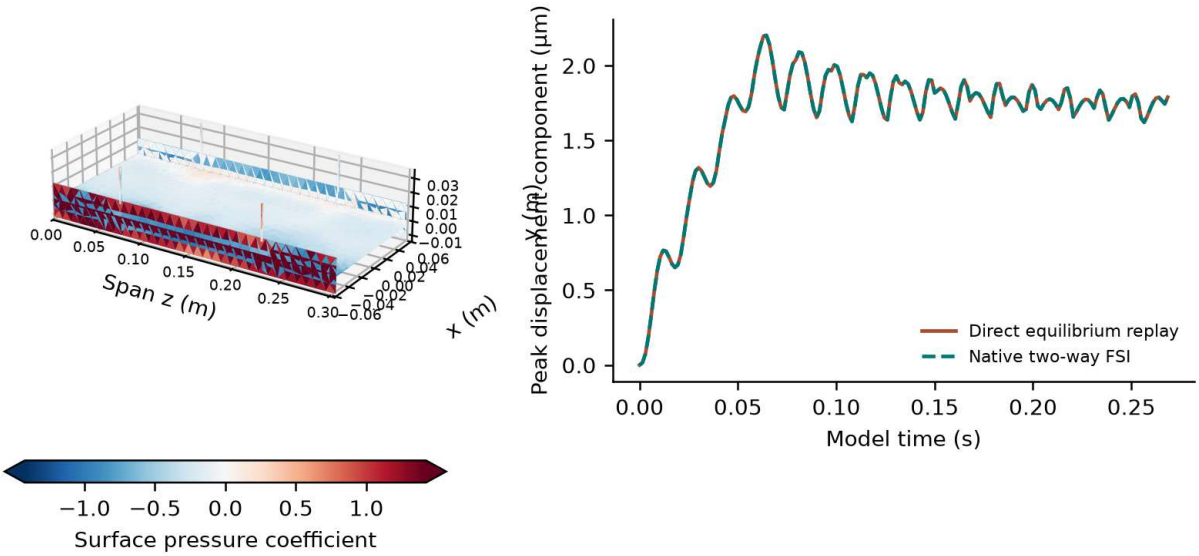

Figure 14. Wetted surface pressure at model time 0.2685 s and the maximum structural displacement component over the saved record. Both displacement curves refer to the same two-bay mesh and the same aerodynamic load history.

The run used a 1.5 ms step, eight partitioned sweeps, ten fluid inner iterations, pseudo-CFL 10 and a 60 ms linear load ramp. The solid used flexible GMRES with ILU fill level 3 and at most 250 iterations per linear solve. We independently assembled the constrained TET4 tangent and consistent mass and replayed nodal pressure and wall shear with a sparse direct Newmark solve. The native peak displacement component was 2.201 μm. At the final frame the native and direct displacement vectors differed by 0.0632% relative to the direct solution in L2 norm. The independent solve checks structural equilibrium for the computed loads. The final mean log10 inter-sweep residuals are -5.38 for air and -11.91 for the solid against the nominal −8 target. The 24.384 mm spatial girder corresponds to Re = 10,160 at the same viscosity.

11.5 Segment airflow and structural motion

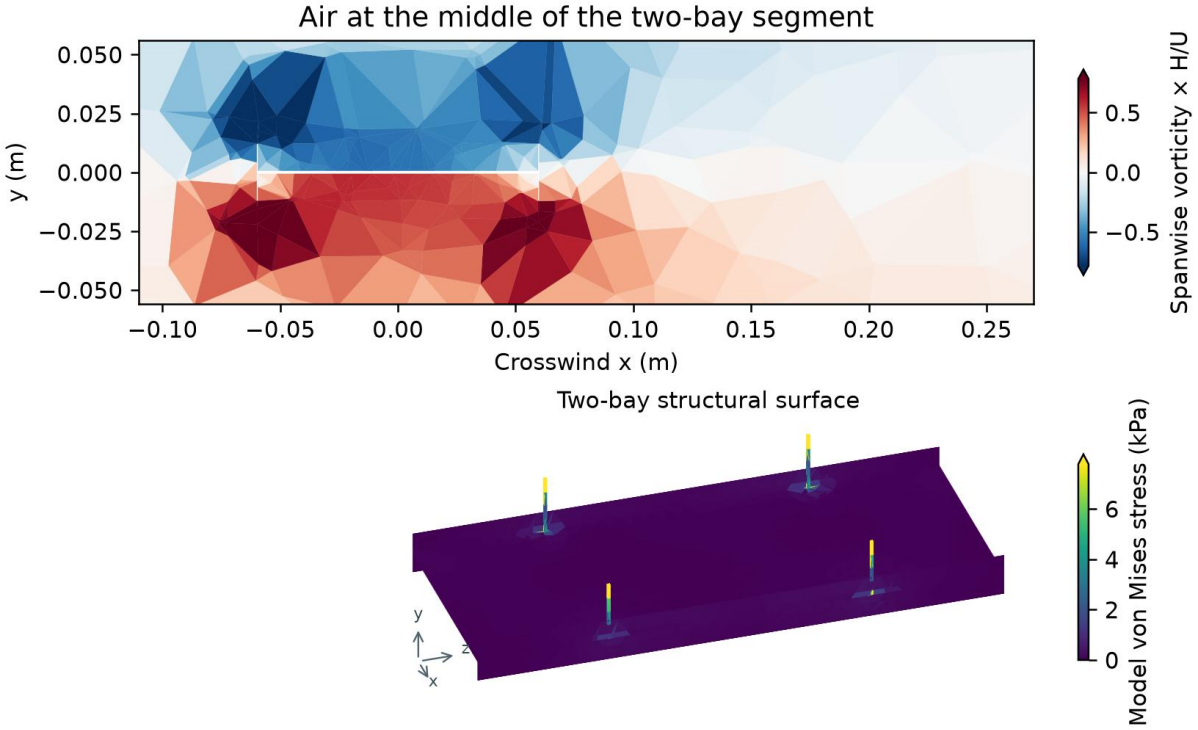

Figure 15. Spanwise vorticity on the central plane of the spatial air mesh and surface von Mises stress on the spatial solid at 0.2685 s model time. The solid is drawn at its calculated displacement scale. The two panels use independent colour scales.

The fluid cut passes through three-dimensional tetrahedra. For each intersected tetrahedron we interpolate vorticity at its plane intersections and average the cut-vertex values for display. The stress view uses native nodal recovery and a face average. Interpretation of local peaks at clamps or material junctions requires material-side recovery and mesh refinement.

11.6 Motion at the three span stations

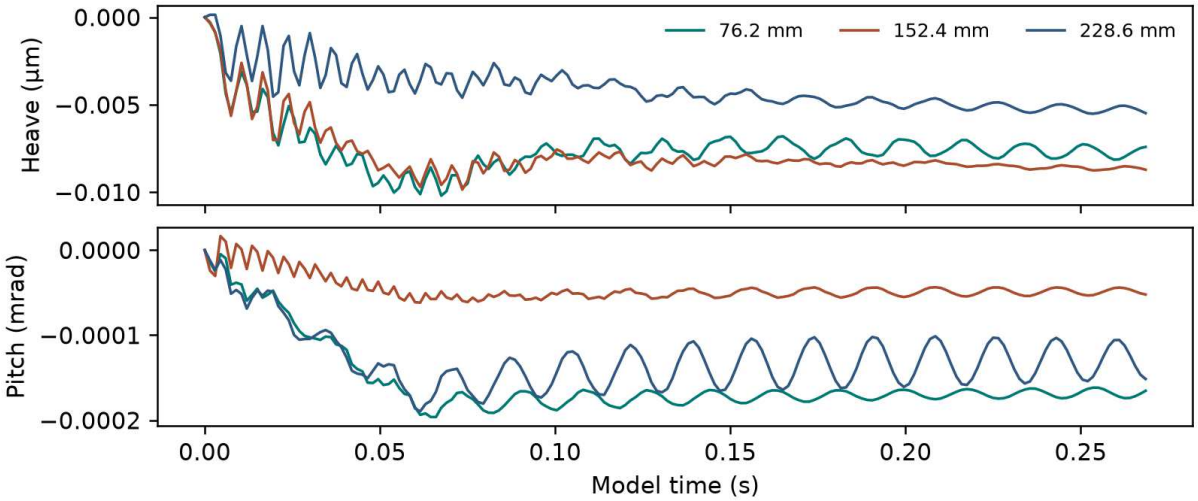

Figure 16. Heave and pitch of three cross-deck chords during the spatial calculation. The legend gives distance from the front cut. Each chord joins slab material points at x = ±48 mm and y = 0 in the reference configuration.

The probes use tetrahedral interpolation independently on both sides of each chord. Midpoint elevation gives heave. The orientation of the deformed chord in the x–y plane gives pitch. Over the common first 0.0105 s, the three-station heave and pitch histories differ by 145.1% and 57.4% in L2 norm relative to the 92,325-fluid-cell mesh. Over that interval the two peak patch tensile stresses are 6.75 and 1.60 kPa, respectively. Over the full pilot record, the largest sampled absolute station heave is 0.0102 µm and the largest absolute chord pitch is 0.000196 mrad. A support or floor-beam displacement would describe a different point of the structure.

For the same material laws and physical supports, the lowest linear-tetrahedron frequencies on the pilot, coarse, medium and fine grids are 57.03, 20.84, 17.50, 14.74 Hz. The medium-to-fine change exceeds 5%. The lowest frequencies above are ordered independently on each mesh. Medium mode 1 pairs with fine mode 2 (MAC 0.613), and medium mode 2 pairs with fine mode 1 (0.785). The fourth medium-to-fine mode has a mass-weighted modal assurance of 0.990 on common material points, but its frequency changes from 61.53 to 54.26 Hz. An independent quadratic-tetrahedron calculation on the pilot and coarse geometries gives 14.07 and 10.73 Hz. It uses six midside nodes per TET4, exact polynomial mass integration and four-point stiffness integration. The native pilot is too stiff for quantitative damage inference. This isolated bridge segment uses local cap supports and free structural end cuts. Its motion cannot identify the antisymmetric torsional mode of the complete suspended main span. The direct comparison in Figure 14 uses a second structural solution driven by the actual fluid history. The spatial FSI itself updates the air grid with the computed segment displacement.

11.7 Concrete patch under transferred loading

The donor supplies 180 boundary frames including the initial state. The OOFEM stress and damage file contains 179 increments, from 0.015 to 2.685 s in prototype time. The donor search is repeated on the actual segment mesh used for this run. Wet face pressure and wall shear act on exposed surfaces. At the slab–beam interface we use the adjoining steel tetrahedron stress tensor and slab-outward normal. The beam traction already includes the startup loading history. On the air side the transfer applies the same ramp used in SU2.

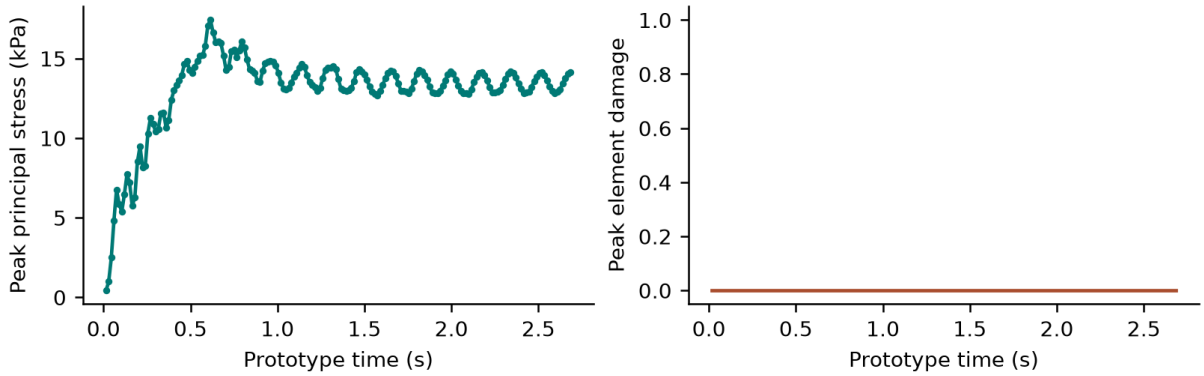

Figure 17. Principal tensile stress and irreversible scalar damage from all 6,144 prototype patch elements. OOFEM used a single stateful history with the trial 3 MPa tensile strength and 100 J/m² crack-band energy.

The maximum principal stress is 17.4 kPa. Maximum element damage is 0, with 0 elements exceeding 10^{-8}. The maximum normalized force-transfer error is 1.08e-12%. The sum of absolute work-transfer differences relative to absolute source work is 1.21e-04%. A separate inertial-frame elastic Newmark replay gives a peak of 17.4 kPa, compared with 17.4 kPa in the corresponding static elastic calculation. This comparison tests the local inertia approximation over the saved frames.

The companion segment movie follows the internal girder and floor-beam cuts, the upper-link stress and the synchronized prototype patch history. The tested patch represents concrete at one floor beam. Its trial material properties, finite loading window and locally supported donor limit its historical interpretation. Connection failure, suspender slackening, steel instability and a changing global tangent are outside this replay. The computed damage variable applies only to this patch under the transferred history.

11.8 Wind speed and the sign of aerodynamic work

Three plane-strain calculations use the same G200 mesh, support modulus, physical step, load ramp and initial orientation. Changing the inlet and initial air speed at fixed viscosity varies Reynolds number with wind speed. The three Reynolds numbers are 4,444, 5,000 and 10,000. The reduced speed uses the computed dry sectional frequency of 1.9057 Hz and the 0.12 m deck width.

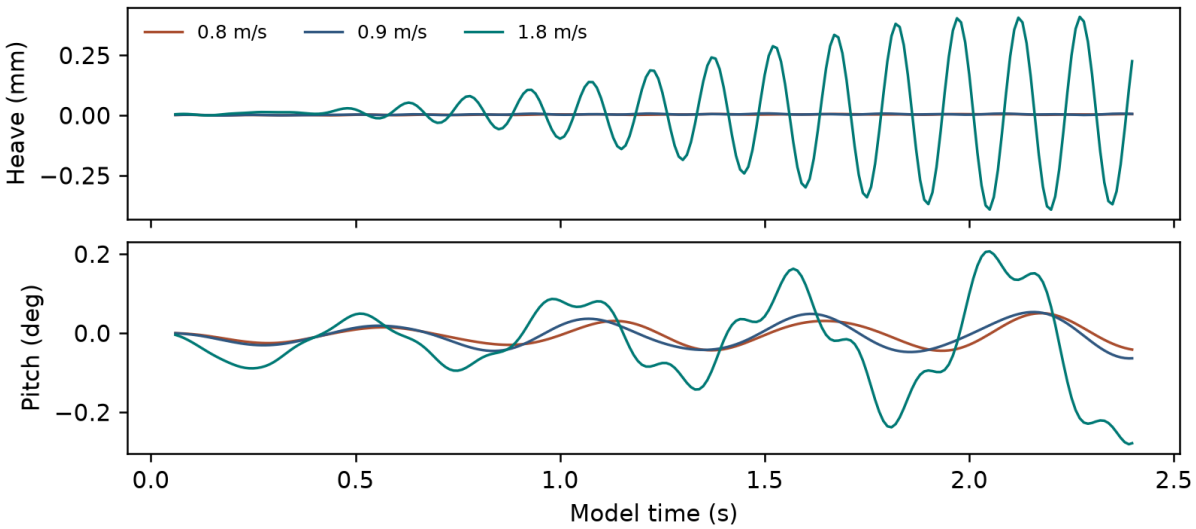

Figure 18. Native two-way sectional responses from model time 0.060 to 2.398 s. The tested 0.8, 0.9 and 1.8 m/s correspond to nominal prototype speeds of 8, 9 and 18 m/s under Froude scaling.

Table 12. RMS values remove the interval mean. The signed pitch work uses the moving-centre moment and dimensional pitch increments over the entire common interval. A finite interval can begin and end at different stored energies.

Model speed	Reduced speed	RMS heave, pitch	Pitch work over window
0.8 m/s	3.50	0.0015 mm, 0.0243°	+4.347e-08 J/m
0.9 m/s	3.94	0.0019 mm, 0.0298°	+9.180e-08 J/m
1.8 m/s	7.87	0.1750 mm, 0.1046°	+1.858e-06 J/m

The dry numerical decay calculation gives a logarithmic decrement of 0.001505 per torsional cycle for the 2 ms step, equivalent to a numerical damping ratio of 0.000239. This estimate uses the eigenvalues of the Newmark amplification matrix for the isolated linear mode. The actual bridge damping and coupled fluid dissipation require separate identification. These three speeds document sensitivity under the assumed supports. They do not bracket a verified flutter onset.

11.9 Spatial refinement under the same incident wind

Four body-fitted fluid meshes and their matching structural meshes resolve the same two-bay solid. All runs start from the same freestream and use a 1.5 ms step, a 60 ms transfer ramp and the same external flow boundaries. This comparison retains eight spatial frames from 0 to 0.0105 s at model scale, equivalent to 0.105 s at prototype scale. At the final common frame only 17.5% of the computed air load is transferred.

Table 13. Peak component of the native segment displacement in model units and peak principal stress anywhere in the prototype patch over a common startup interval. Peak displacement is the largest absolute Cartesian component anywhere on the donor mesh. The last columns come from separate OOFEM histories registered to each donor.

Grid (fluid / solid cells)	Peak displacement	Patch tensile stress	Peak damage
Pilot 10,614 / 6,805	0.723 µm	6.75 kPa	0
Coarse 92,325 / 33,818	0.957 µm	1.6 kPa	0
Medium 218,923 / 59,701	0.872 µm	1.97 kPa	0
Fine 532,244 / 108,699	0.884 µm	1.29 kPa	0

For three fixed measurement chords, the medium-to-fine relative L2 differences are 28.8% in heave and 48.0% in pitch. The normalizations use the fine-grid histories over the same eight frames. The histories retain their measured signs. Changing both the flow and structural mesh changes both tractions and compliance, so the table measures their combined effect.

The independent dry comparison helps interpret that sensitivity. The lowest native linear-tetrahedron frequency decreases from 57.03 Hz on the pilot to 14.74 Hz on the fine grid. Test functions with quadratic interpolation on the coarse geometry lower the first frequency further. The large shifts with mesh density and interpolation order identify bending compliance as a source of uncertainty in stresses transferred from the donor. These startup comparisons do not determine the stress reached during the historical failure.

11.10 Air loads and support reactions on the two-bay segment

The native three-dimensional flow solver integrates pressure and viscous traction over the monitored deck boundary. Positive x points downwind, positive y is upward and positive z runs along the span. The moment is about the spanwise axis through the fixed origin. The plotted loads are for the full two-bay model, with the structural startup multiplier applied.

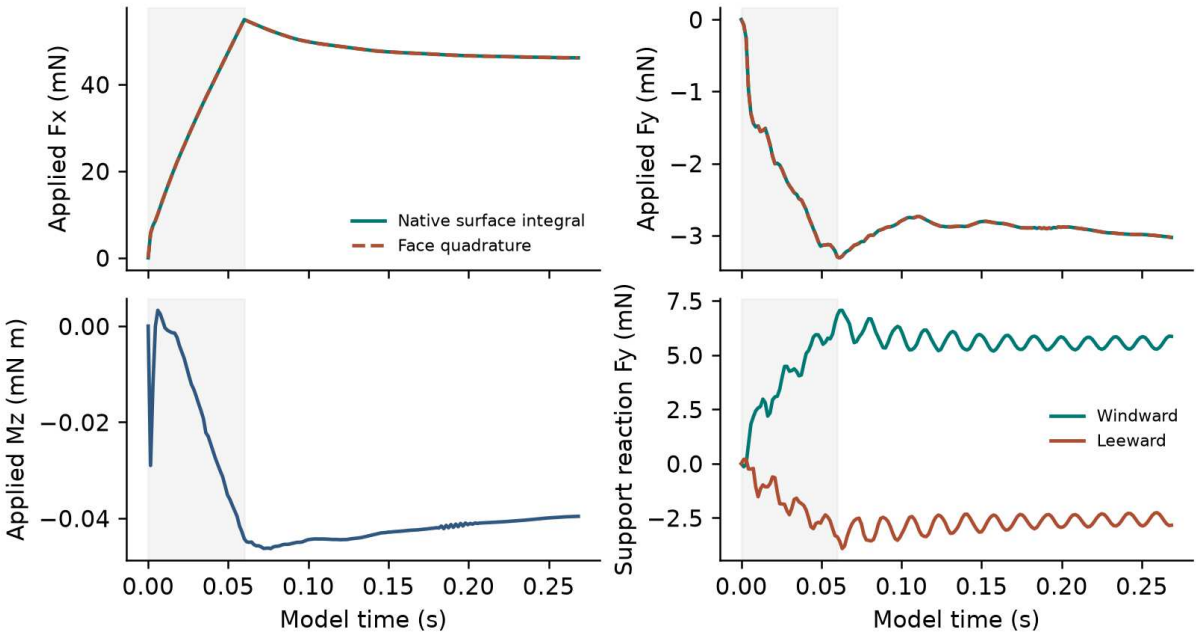

Figure 19. Model-scale horizontal and vertical air forces, twisting moment, and vertical reaction exerted by the two pairs of supports on the segment. Shading identifies the first 60 ms. The dashed curves integrate the saved moving-face fields independently. Ordinates retain their signs.

Peak absolute vertical force reaches 3.31 mN and peak absolute twisting moment reaches 0.0463 mN m. The relative L2 difference between the two integrated three-component force histories is 0.00873%, with the native force history as denominator. The independent integral omits fixed cap faces and uses linear face interpolation of the saved nodal tractions.

The structural replay recovers the constrained rows of the consistent mass and stiffness matrices. For each frame the cap reaction is the sum of elastic and inertial nodal forces less the external traction on constrained degrees of freedom. Across all frames the largest norm of the applied force plus support reaction less total inertia is 4.50e-12 N. This checks equilibrium of the replay under its own transferred loads. It does not calibrate the hanger and cable stiffness of the historical bridge.

11.11 What a spanwise-uniform load can excite

To test whether a single sectional load trace can reproduce the observed reversal of twist at midspan, we applied the G200 lift and fixed-origin pitching moment uniformly along the suspended main-span tangent of Section 7. The sectional histories retain their measured signs, timing and startup multiplier. Each free station receives the line load times its tributary length. Each pinned end carries the remaining half bay. The calculation starts at rest and retains all 55 modes in each coordinate family. The prescribed loads have no feedback from the span, and the concrete replay uses the separate three-dimensional donor.

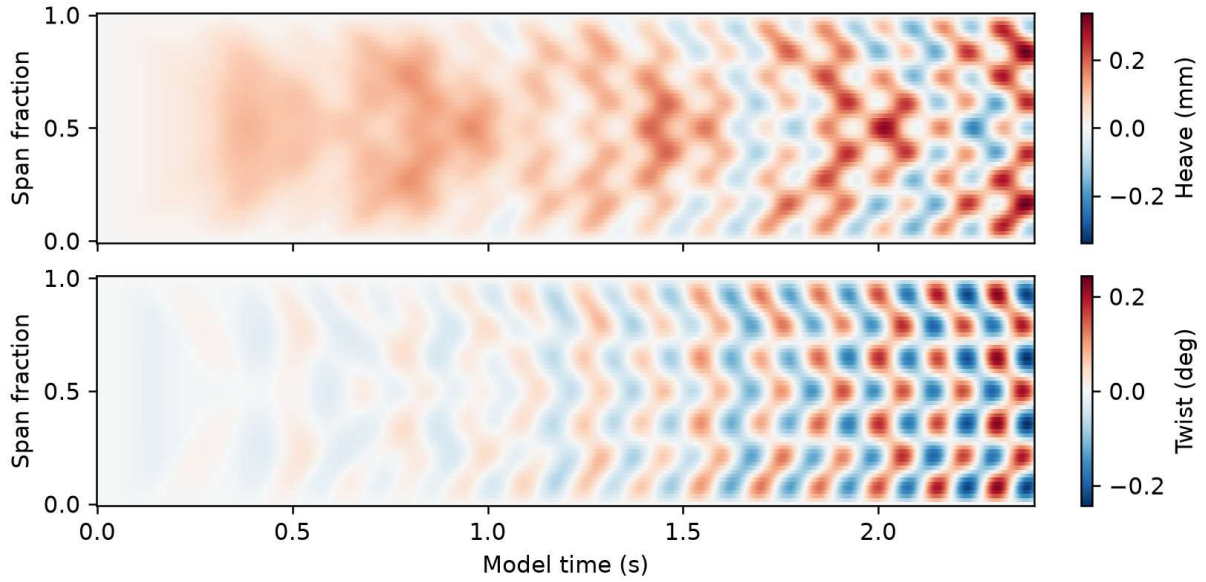

Figure 20. Heave and twist along the full 8.5344 m scaled main span under prescribed uniform sectional loading. The horizontal coordinate is time. The vertical coordinate runs from one tower to the other. Colour shows response with zero assumed physical damping.

The first dry torsional mode changes sign across midspan. Its generalized force is proportional to the signed sum of its modal ordinates under uniform loading. The magnitude of that signed sum is 4.8e-15 times the sum of their magnitudes. The two quarter-span twists therefore track each other under this loading. Opposite quarter-span rotations in the historical event require a mechanism that breaks this symmetry or introduces an antisymmetric disturbance and motion-dependent aerodynamic work.

The largest computed heave and twist are 0.339 mm and 0.243°. An assumed 0.5% modal damping ratio gives 0.316 mm and 0.210°. Halving the constant-average-acceleration step from 2 to 1 ms changes the undamped full-record displacement norms by 0.46% and 0.91%, respectively, with linear interpolation of the same measured loads. Historical damping and spanwise loading remain unidentified.

11.12 Deformation of the equivalent sectional supports

For every saved planar frame we reconstructed each reference-triangle displacement gradient and the signed deformed-to-reference area ratio. A nonpositive ratio identifies element inversion. We applied the same orientation check to the moving air triangles. This test examines local support deformation even when fluid mesh checks and the solver exit status indicate success.

In the finite-deformation check, F is the identity plus the reference displacement gradient and J is its determinant. Plane strain imposes a unit out-of-plane stretch. The stored energy per reference volume and its Cauchy stress use the two Lamé constants of Eq. (7) and zero thermal strain [7].

$$W = \frac{G}{2}[tr(\mathbf{F}^{\mathsf{T}}\mathbf{F}) - 3 - 2\ln J] + \frac{\lambda_L}{2}(\ln J)^2 \tag{19}$$

$$\boldsymbol{\sigma} = \frac{1}{J}\frac{\partial W}{\partial \mathbf{F}}\mathbf{F}^{\mathsf{T}} = \frac{G}{J}(\mathbf{F}\mathbf{F}^{\mathsf{T}} - \mathbf{I}) + \frac{\lambda_L \ln J}{J}\mathbf{I} \tag{20}$$

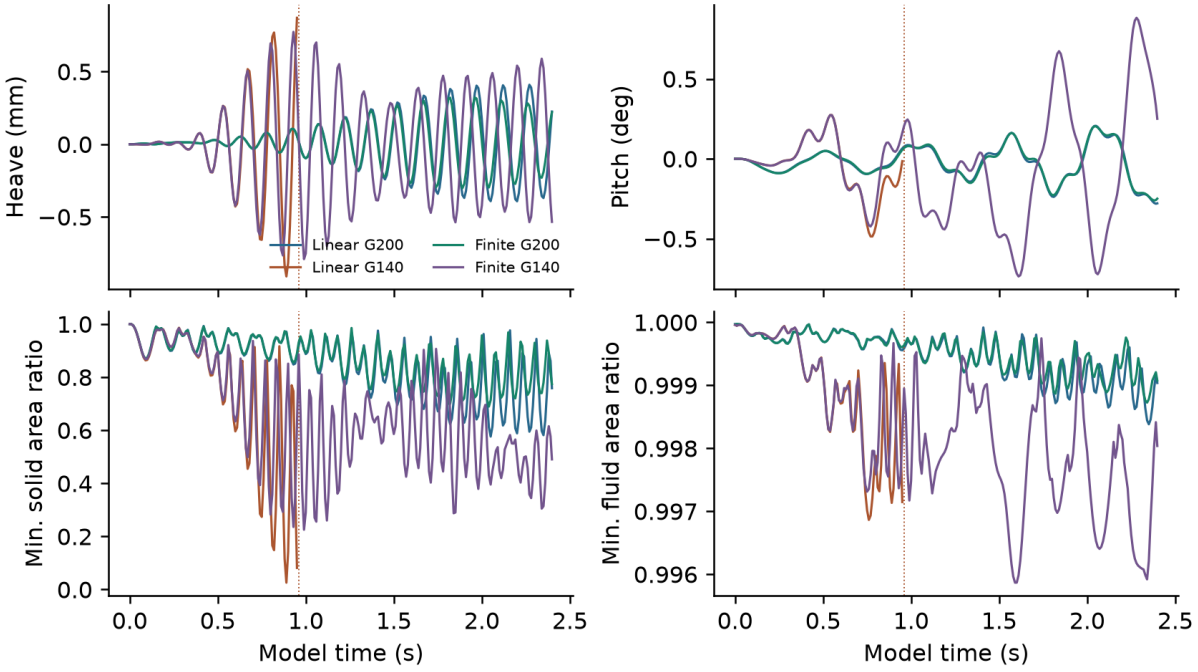

Figure 21. Rigid-fit deck motion and minimum signed area ratios at 1.8 m/s. Each curve stops at the last saved frame preceding any solid inversion. The vertical dotted line marks the first inverted frame of the linear G140 support model.

On G200, the maximum absolute principal small strain in the soft inserts reaches 49.9%. On G140, the first saved inverted solid triangle occurs at 0.960 s, although the minimum air area ratio stays above 0.992 across the entire record. Subsequent linear G140 frames are excluded from physical interpretation. At 0.8 and 0.9 m/s, the linear G200 inserts reach 4.4% and 5.3% strain, respectively, with positive signed areas.

The finite-deformation runs use the TENSORA compressible neo-Hookean option in both regions, retaining each region's original density, Poisson ratio and initial Young modulus. The structural inner iteration limit is 10. Minimum signed structural area ratios are 0.689 on G200 and 0.225 on G140. Relative to the G140 history, the post-ramp L2 differences between G200 and G140 are 113.6% in heave and 121.7% in pitch through 2.398 s. The G140 peak heave and pitch over the positive-area interval reach 0.791 mm and 0.882°. Both meshes preserve positive element areas throughout the saved histories. Successive upward mean-pitch crossings define 4 intervals, with positive pitch work in 2. One interval lasts only 0.091 s, so these crossings do not establish a single modal period. The finite-strain G200 record instead has positive work in all three crossing intervals.

11.13 Where the twisting moment comes from

A pressure difference between the two edges can twist the deck even when its net lift is small. A vertical force on the downwind edge has a positive lever arm about the spanwise axis through x = y = 0. The same upward force on the windward edge has a negative lever arm. Horizontal traction also contributes when it acts above or below that axis. For Figure 22, Eq. (5) uses a fixed origin. The pitch-work histories in Table 12 instead use the moving deck centre.

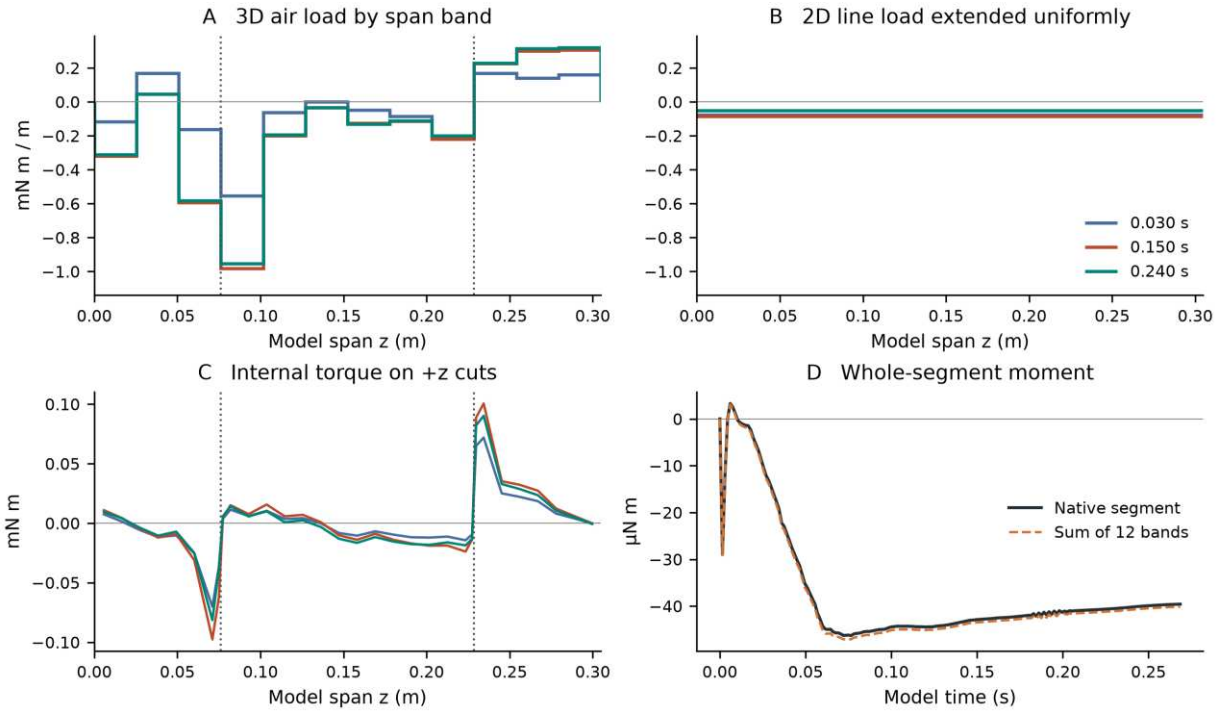

Figure 22. Applied aerodynamic moment per unit span in twelve 25.4 mm bands (A) and the corresponding G200 plane-strain value repeated along the span (B). Both use the same fixed axis, units and startup multiplier. Panel C gives the internal torque carried across 32 positive-z solid cuts, in mN m. D compares the integrated 3D surface moment with native SU2 output. Dotted vertical lines locate the floor beams.

Plane strain enforces spanwise uniformity and suppresses longitudinal shear strains. Its line load has no independent span coordinate. In the two-bay model, floor beams and links interrupt the deck geometry, pressure can vary along the span, and shear can flow through the slab and girders into the supports. Equation (16) integrates that shear stress over a cut. Changes of internal torque between cuts also reflect inertia and support reactions. The air load on a band and the torque transmitted across its end are different observables.

At 0.150 s the planar line moment is −0.086 mN m/m. The 3D bands range from −0.983 to +0.305 mN m/m. Cancellation, defined as one minus the magnitude of the band sum divided by the sum of band magnitudes, is 50.6% at that instant. The resultant is −43.48 μN m, compared with −42.87 μN m from SU2. We clipped the moving faces by reference span station, integrated pressure and viscous moment on each piece, and checked all 180 frames. The relative L2 discrepancy is 1.66%. Both grids and support systems differ between the models. The asymmetric band pattern from this coarse transient cannot by itself identify a physical spanwise instability.

11.14 Reading a wake through a pitch cycle

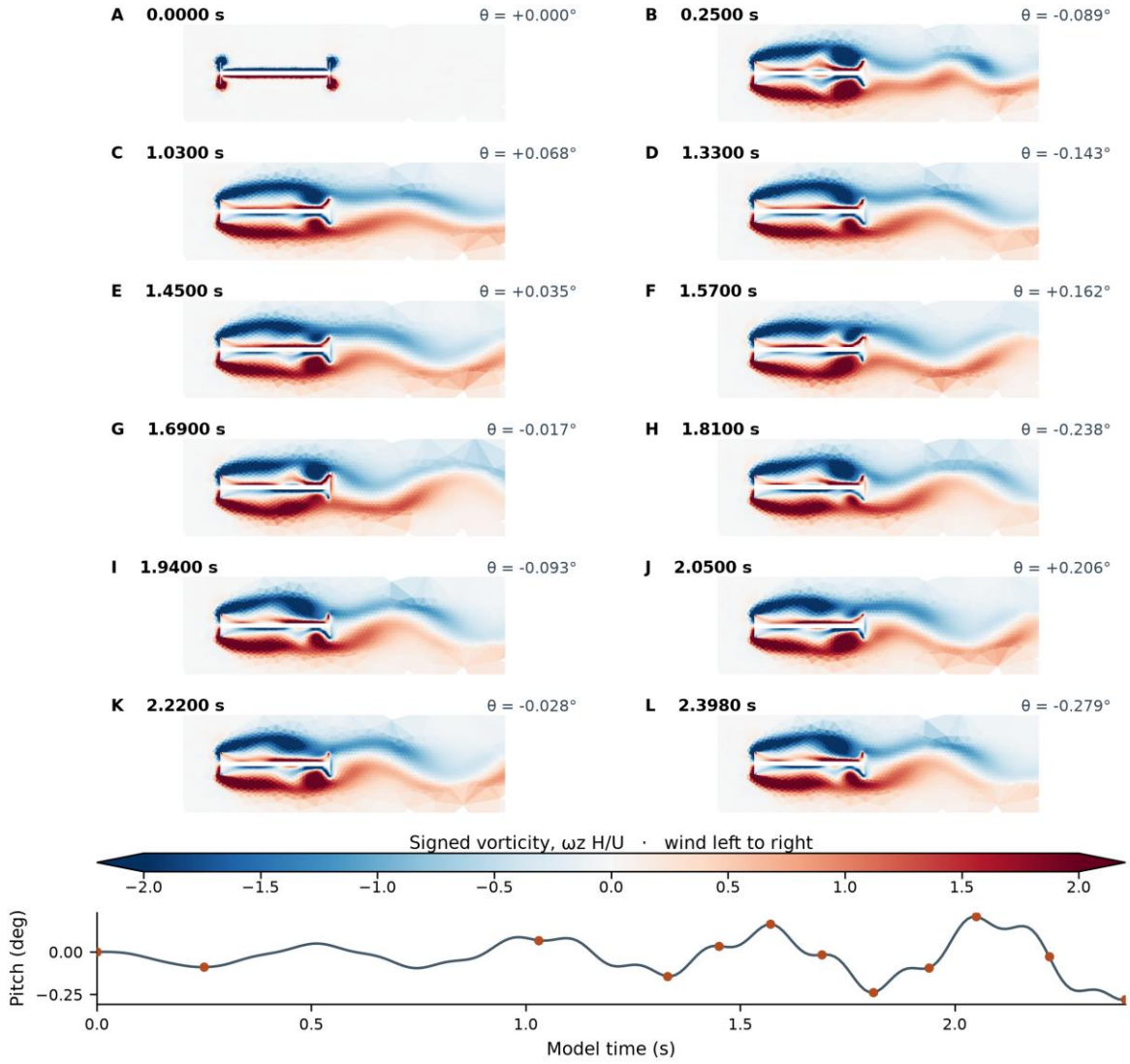

Figure 23. Twelve native frames from the linear G200 plane-strain animation. Read from left to right, then down. Each panel spans x = −0.10 to +0.25 m and y = ±0.053 m at model scale. All use the same signed vorticity limits. The orange dots show the selected times on the full pitch history. Nine frames lie at or after 1.330 s.

At startup the strongest shear is confined to the girder edges. Downstream, the upper and lower layers bend into the wake. Between F and H, pitch changes from +0.162° to −0.238° as the wake bends downstream; the fluid seen farthest to the right left the deck earlier. Vorticity locates rotation in the fluid. Pressure and wall shear supply the actual force. The sign of pitching power depends on whether moment and angular velocity point the same way. Integration about the moving deck centre gives +0.14, +0.78 and +0.99 μJ/m in three full G200 crossing intervals. The support sensitivity in Section 11.12 limits what those signs establish about flutter [3, 6].

11.15 Pressure during the spatial load ramp

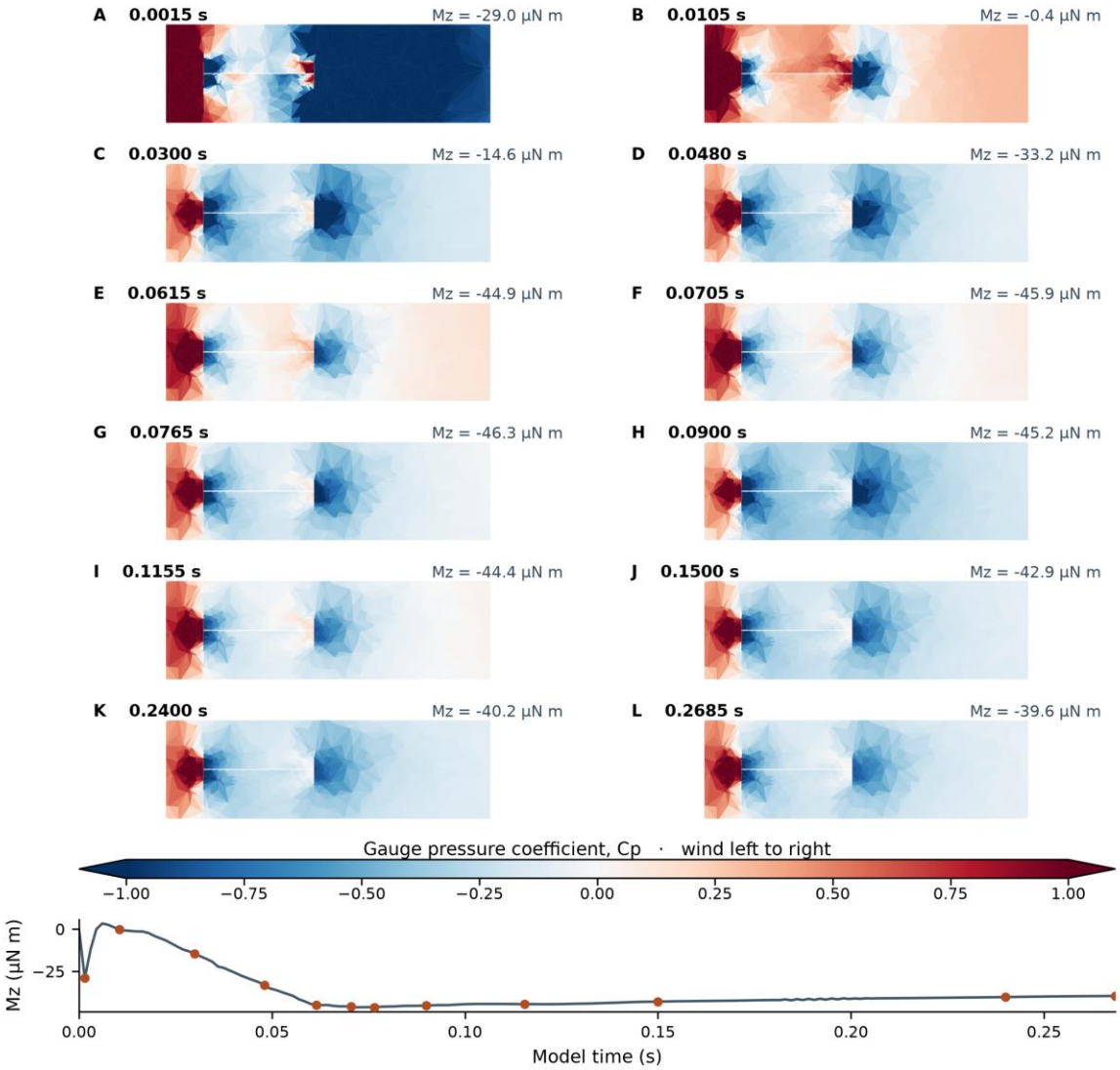

Figure 24. Gauge pressure in the three-dimensional fluid at z = 152.4003 mm, halfway between the two floor beams. Each panel has the same x–y extent as Figure 23. Pressure is divided by the inlet dynamic pressure of 2.020 Pa. The annotation gives the applied moment on the entire two-bay deck. The solid stress plates use the same twelve saved states.

Windward stagnation raises the pressure, while suction near the deck edges shifts the resultant and its lever arm. Panels A–D cover the load ramp. The coloured pressure field is the fluid solution; the startup multiplier acts on the load passed to the solid. At E the full load is active. The most negative whole-segment moment occurs at G, 0.0765 s. The central pressure plane samples one station, while the annotated moment includes the pressure and shear around all wetted moving faces. The streamwise pressure contrast persists even as the net torque relaxes.

11.16 Looking inside the two-bay segment

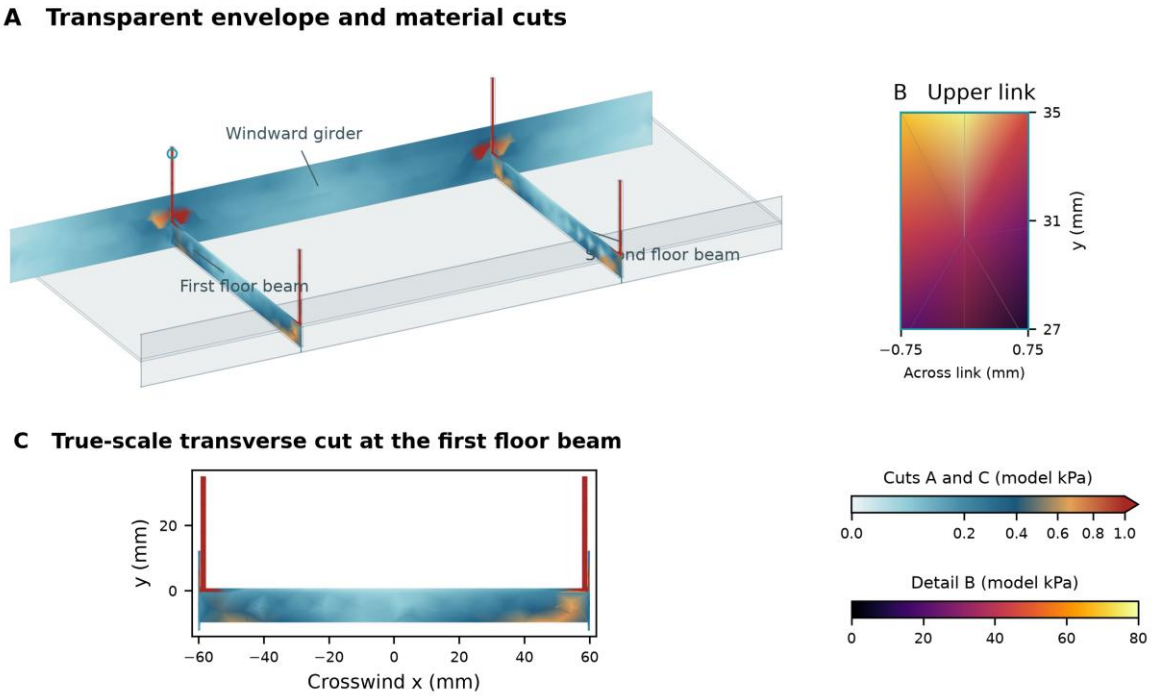

Figure 25. At 0.0615 s model time, the light transparent shell locates three true cuts through the structural tetrahedra. The longitudinal cut passes through the windward girder at x = −59.800 mm. The transverse cuts cross the two floor beams at z = 76.201 and 228.601 mm. A cyan ring locates the windward link selected for the enlargement. C shows the first transverse cut at equal horizontal and vertical scale.

The beam carries deck load across the roadway to the two girder lines. The links terminate at fully fixed caps in this model. A change of direction in the load path, a small steel section and the imposed restraint can all raise local stress. The elevated stress near a cap is therefore sensitive to how the connection is idealized.

In B the selected portion of the actual cut is 1.5 mm wide and extends from y = 27 to 35 mm. Its width is enlarged relative to height so that the stress gradient and interpolation triangles can be read. The two scales serve different physical ranges. A and C resolve lower stresses in the slab and girder at 0–1 kPa; B resolves the link over 0–80 kPa. These fixed scales carry through Figure 26 and the updated movie. Geometry is shown at reference coordinates. Colour is the native recovered von Mises stress interpolated through solid tetrahedra.

11.17 Stress through the floor beams and upper link

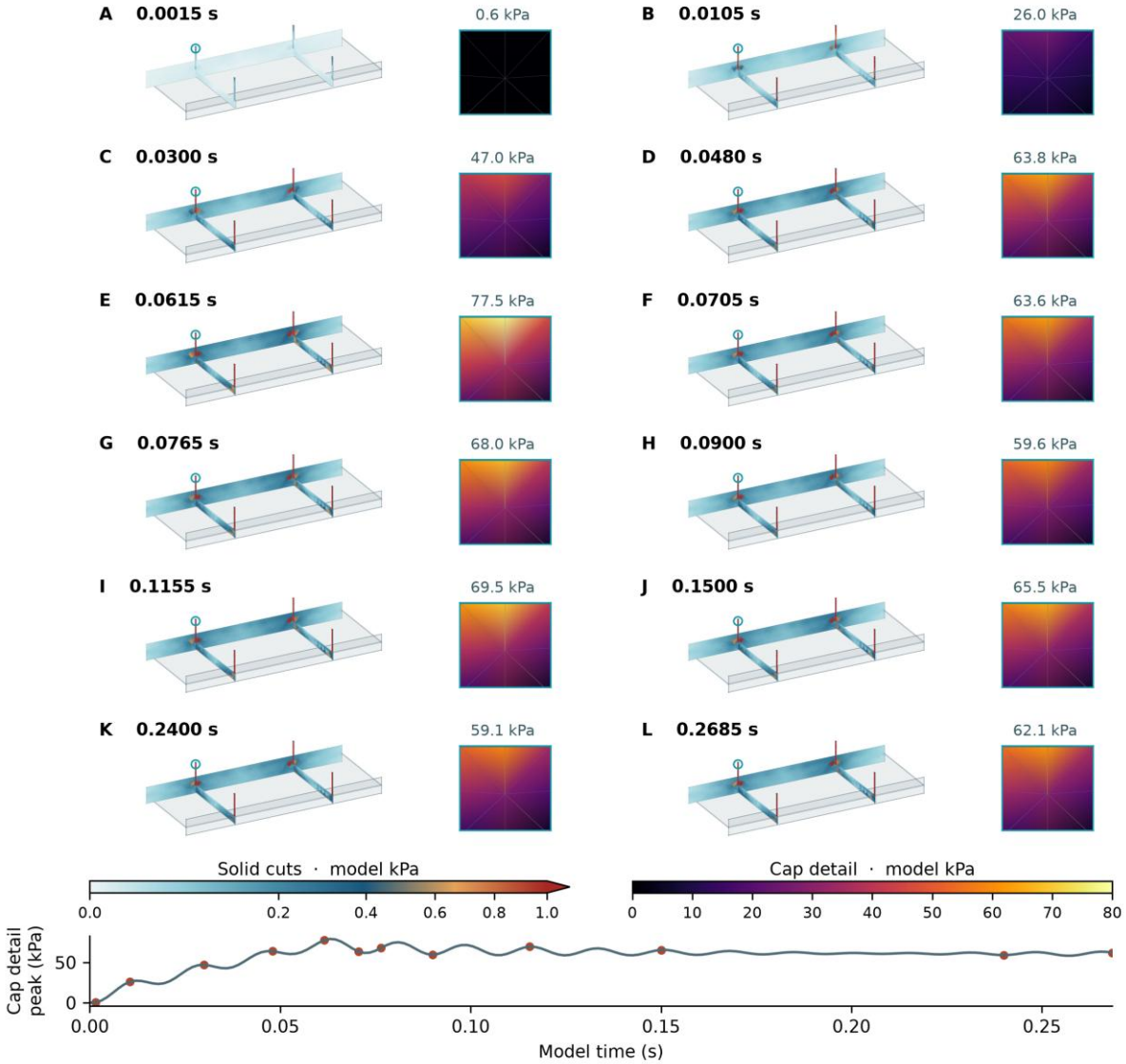

Figure 26. Synchronized cutaway views of the two-bay solid. Left in each panel, the transparent envelope shows the positions of the girder and floor-beam cuts. Right, the windward upper-link detail uses its own fixed linear colour scale. The number above it is the largest interpolated stress among the cut vertices inside that window. The curve below tracks this same observable over all 180 frames.

The selected cap stress increases from 0.6 kPa at A to 77.5 kPa at E, drops to 63.6 kPa at F, and rebounds to 68.0 kPa at G. The largest applied twisting moment in magnitude occurs at G rather than E. Individual members also carry drag, lift, support reactions and inertial load. A local equivalent stress need not peak with a global moment. Von Mises stress measures distortion and has no tension or compression sign. The following plate therefore examines principal stress in the concrete separately.

11.18 Tensile stress within the concrete patch

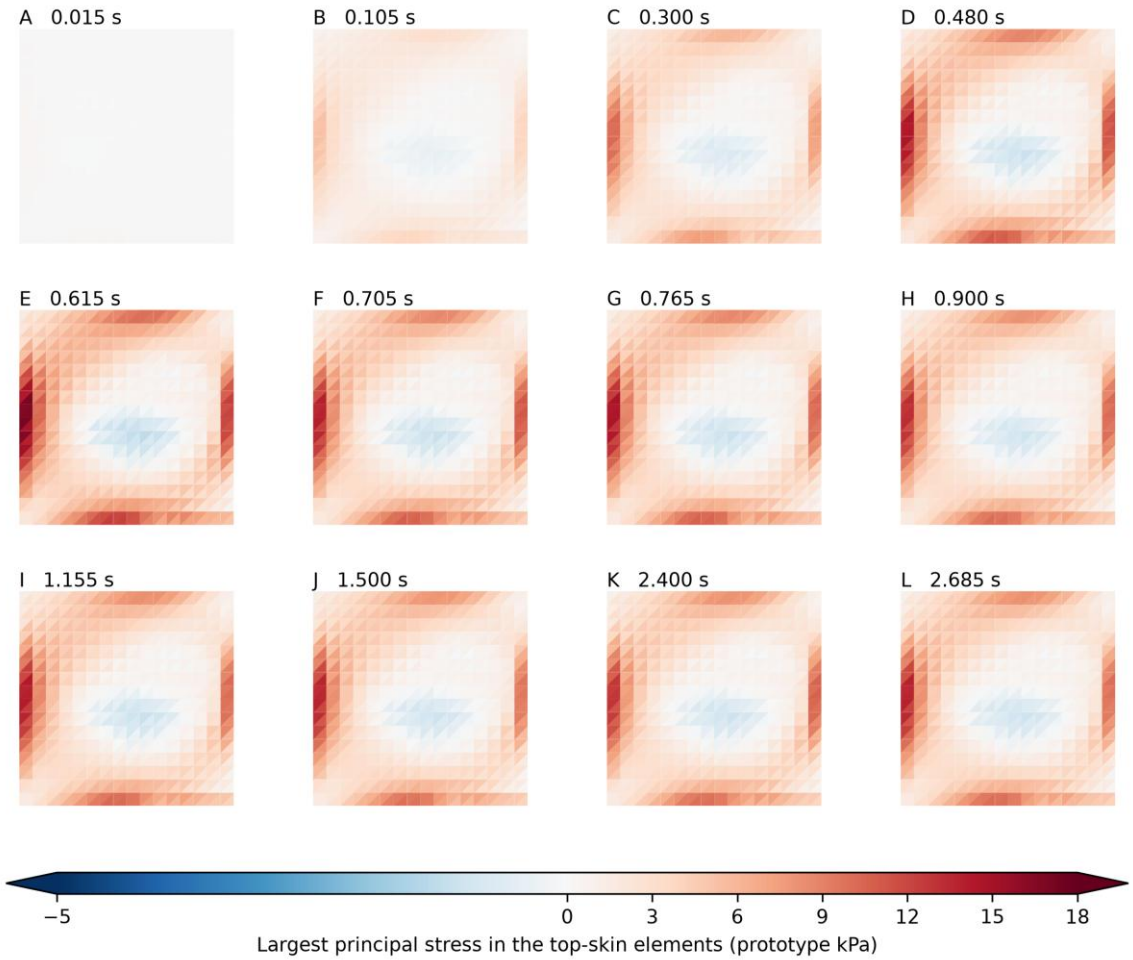

Figure 27. Largest algebraic principal stress in the 512 tetrahedra adjoining the upper skin of the 1.2 m square concrete patch. Each triangle has its owner's cell stress. A–L match Figures 24 and 26. The labels here use prototype time, ten times the model time. The view looks down on the patch; x increases to the right and z upwards, both from −0.6 to +0.6 m. Red denotes tension. Blue means that all three principal stresses are compressive.

As the patch deforms, tension develops near parts of the perimeter and a small central region carries compression. At E, 0.615 s prototype time, the most tensile upper-skin cell reaches 17.11 kPa; the largest value across all 6,144 cells is 17.42 kPa. The local stress then unloads and reloads. Damage stays zero for the specified trial material over this history. The replay includes no fatigue law or accumulated service-load history, so it provides a stress history for discussing cyclic demand and leaves fatigue life undetermined.

11.19 Why a single section misses antisymmetric torsion

Let z run from one tower to the other and take positive twist about the same fixed span axis at every station. The wind can generate a clockwise or counterclockwise pitching moment on a plane section. Its sign can reverse over time. Antisymmetry along the bridge asks a different question. At the same instant, do mirror stations twist in opposite directions? For a dry antisymmetric twist shape φ, the rotations at z and L − z have opposite signs. With m the applied aerodynamic moment per unit length, its odd part is

$$m_o(z,t) = \frac{m(z,t) - m(L-z,t)}{2} \tag{21}$$

A virtual rotation proportional to φ gives a generalized force equal to the integral of mφ. Pairing mirror stations reduces that integral to half the span,

$$Q_o(t) = \int_0^{L/2} \phi(z)\,[m(z,t) - m(L-z,t)]\,dz \tag{22}$$

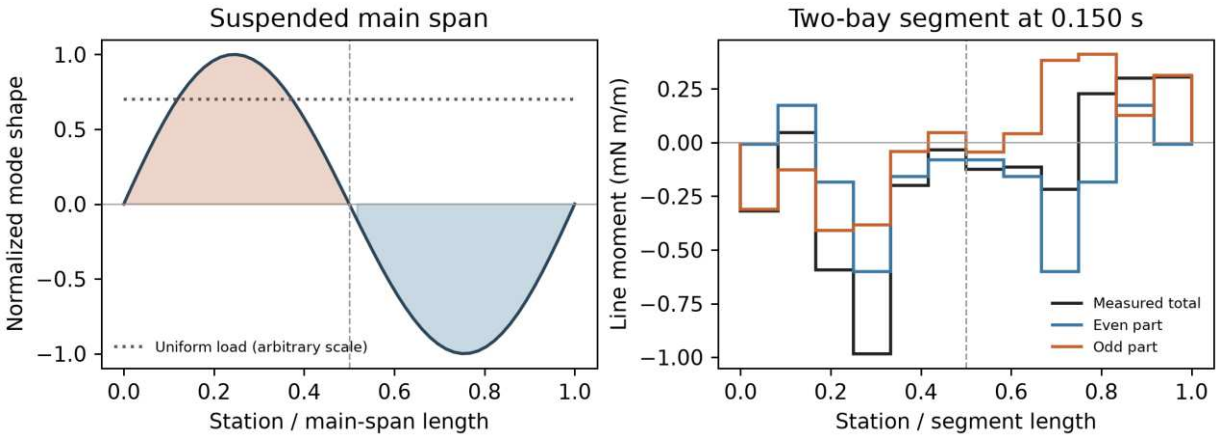

Figure 28. Left, first dry torsional mode of the suspended main span (1.869 model Hz), normalized to unit peak. A uniform applied line moment gives opposite work contributions on the two shaded lobes. Right, the measured two-bay line moment and its even and odd parts about the midpoint of that shorter segment at 0.150 s.

The independent planar solution supplies one m(t). Repeating it at every station makes each bracket in Eq. (22) vanish. In the discrete span model the residual projection is below 5×10^{-14} of the sum of absolute contributions. Uniform mean wind can still feed a seeded odd motion. For example, a local moment proportional to angular velocity gives modal work proportional to the span integral of the squared mode shape when its coefficient is positive. That feedback requires station-dependent deck motion.

In the twelve local bands the odd component has 69.8% of the total Euclidean norm at this instant. This measures variation about the segment midpoint. The 0.3048 m segment has different boundaries from the 8.5344 m suspended span. Internal torque across a solid cut also has its own spatial symmetry. For example, in uniform Saint-Venant torsion it depends on the twist gradient, which is even for an odd rotation field.

11.20 Stress as the plane-strain deck pitches

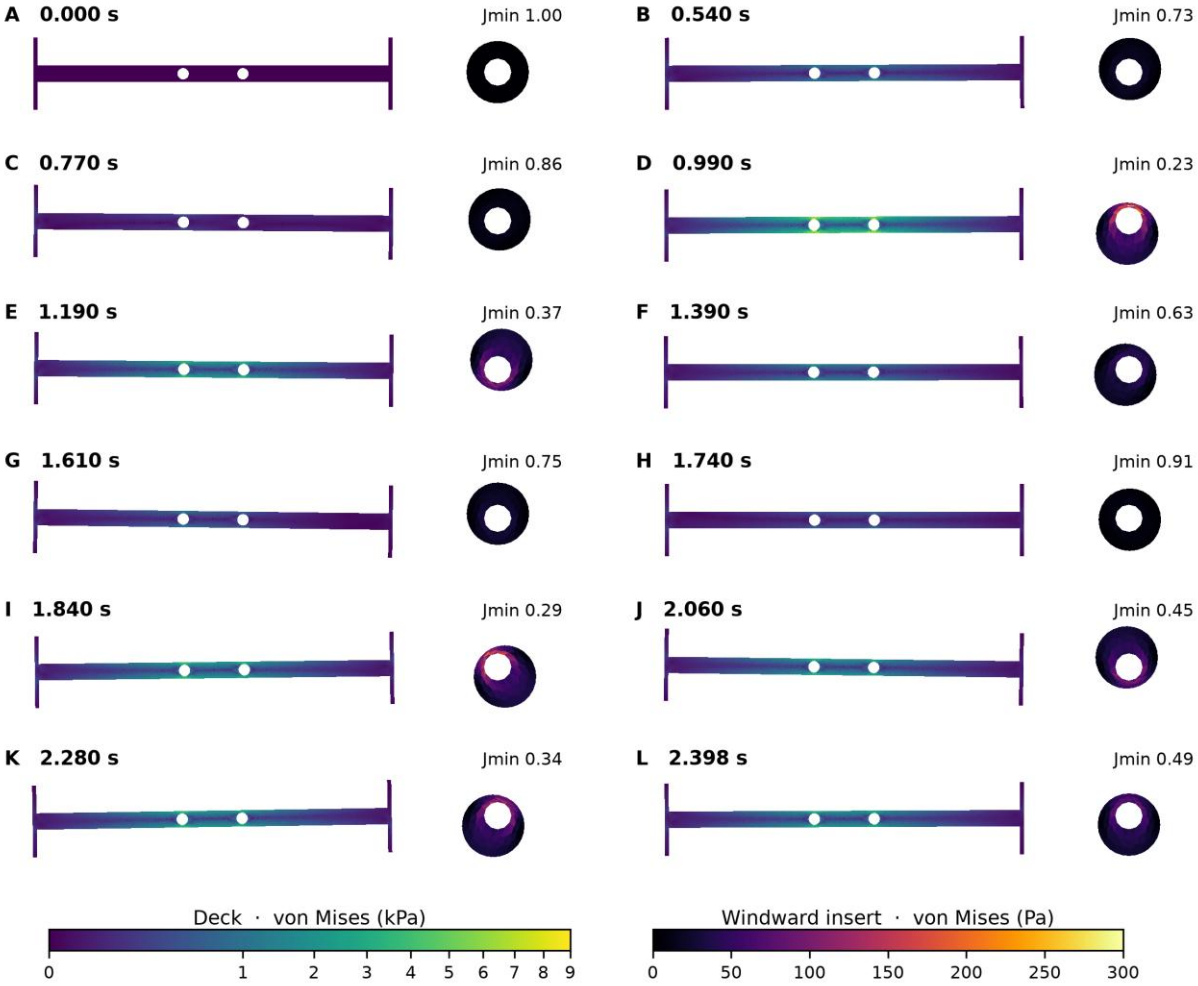

Figure 29. Twelve saved states of the independent finite-deformation G140 plane-strain model. Each left view covers the 120 mm deck and each right view enlarges its windward insert. Both use the actual deformed coordinates. The two fixed colour scales resolve the stiff deck (kPa, power exponent 0.45) and the soft insert (Pa, linear). The labels give the minimum element area ratio across the section. All times are model seconds.

The stress field is recovered separately in every three-node structural triangle from the saved nodal displacement gradient. Setting the span stretch to one in Eq. (20) retains the out-of-plane Cauchy stress in the three-dimensional deviator used for von Mises stress. Element colours preserve jumps across material boundaries. At 0.540, 0.990 and 2.398 s we also averaged each stress component onto nodes belonging to one material only. Across both regions the largest relative L^2 difference from the native nodal output was 2.10×10^{-7}.

At 0.990 s the deck reaches 8.68 kPa equivalent stress and the larger peak across both inserts is 293 Pa. The section-wide minimum area ratio falls to 0.225. A stiff deck can carry the higher stress while a much softer support accommodates the larger distortion. By 2.398 s the deck peak is 4.23 kPa and the insert peak is 89.4 Pa. The continuing crosswind still loads the structure at this last frame.

11.21 What the material laws predict

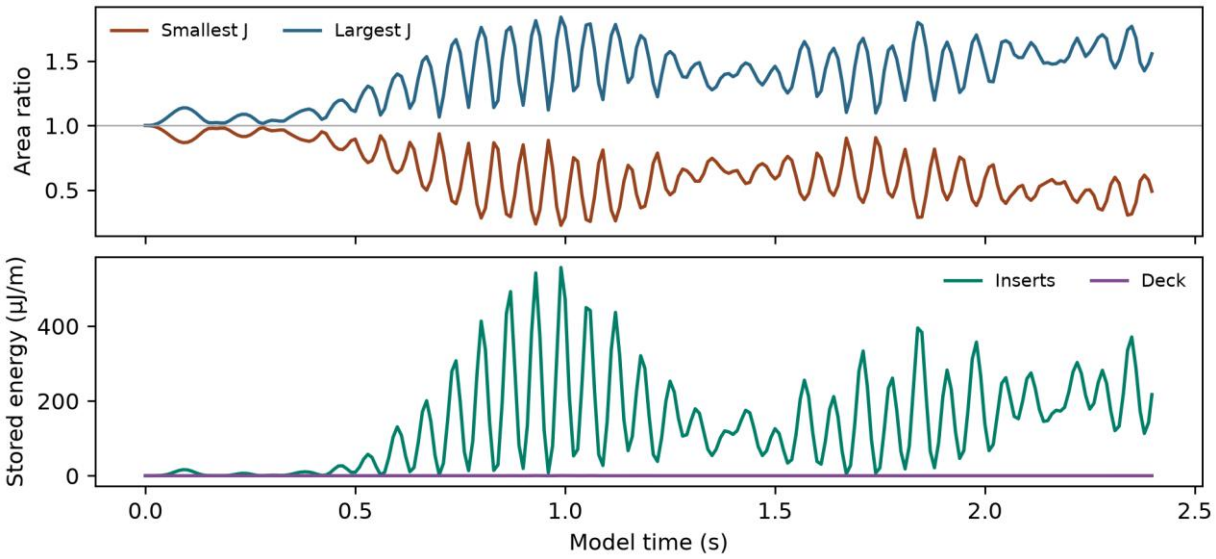

Figure 30. Element area extrema and recoverable strain energy per metre of model span in the G140 plane-strain run. Energy is integrated over the reference triangle areas for the deck and for both inserts. The two quantities share one energy scale.

Table 14. Constitutive assumptions and available response variables. The first two rows use model-scale properties. The patch uses prototype properties.

Calculation	Material law and parameters	Meaning of its output
2D finite-strain deck and inserts	Compressible neo-Hookean. Deck E = 2.10 GPa, ν = 0.30. Inserts E = 97.44 Pa, ν = 0.35.	Stress follows the current deformation gradient. Stored energy is recoverable under material unloading.
3D two-bay FSI	Isotropic linear elasticity. Steel E = 2.10 GPa, ν = 0.30. Slab E = 0.300 GPa, ν = 0.20.	Small-strain model-scale stresses, including signed longitudinal stress in the slab.
Prototype concrete replay	OOFEM idm1 isotropic damage. E = 30 GPa, ν = 0.20, tensile onset strain 0.0001, fracture energy 100 J/m².	Maximum historical Rankine equivalent strain drives scalar tensile damage with exponential softening [8].

At 0.990 s the two inserts store 557 µJ/m and the deck stores 0.379 µJ/m. The energy measures the area under a reversible material loading curve. Finite strain enters through the changing deformation gradient and its determinant. Neither elastic law evolves plastic strain or a yield surface. The energy remaining in the driven system at the end of the run cannot quantify a permanent set.

For the undamaged trial material, positive maximum principal stress divided by E gives the Rankine equivalent strain [8]. Inferred from the archived stress maximum, its peak is 5.81×10^{-7}, or 0.581% of the onset strain. The recorded damage variable stays at zero across the 6,144 tetrahedra through 2.685 s prototype time. This checks damage initiation for this short boundary history and trial material. Fatigue accumulation would require a separate history-dependent law and service loading.

11.22 Air moving along the two-bay deck

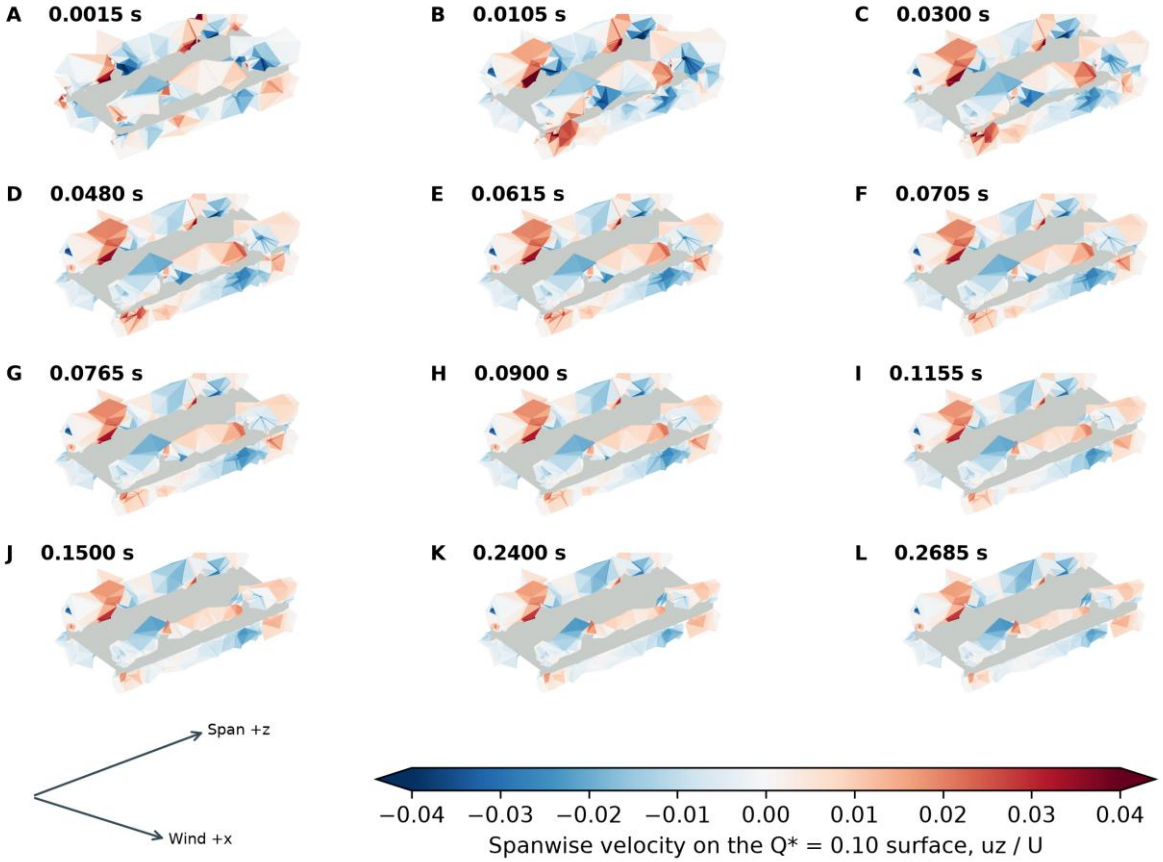

Figure 31. Twelve views of a constant positive Q surface extracted from the three-dimensional air mesh around the grey moving deck. The observer looks down obliquely. Increasing span z points up and right, and the crosswind points down and right. Blue and red show negative and positive span velocity on the same surface. Model times match the structural cuts in Figure 26.

The plotted surface marks $Q(H/U)^2 = 0.10$, with H = 24.384 mm and U = 1.8 m/s. For incompressible flow, Q is half the difference between the squared rotation-rate and strain-rate tensor norms. A positive value picks out air where local rotation exceeds strain. We intersected the native nodal field with each moving fluid tetrahedron and interpolated span velocity on the crossing edges. Only the near-deck region is displayed.

At 0.150 s the surface contains 2,989 triangles. Their mean interpolated span velocities range from −0.0665 U to +0.0611 U. Colours saturate at ±0.04 U in every frame. The two signs show air moving both ways along the span even with a crosswind inlet. The angular facets reflect the local mesh. The threshold, short duration and coarse grid limit interpretation of individual vortices or shedding coherence.

11.23 Comparing the wake at matched locations

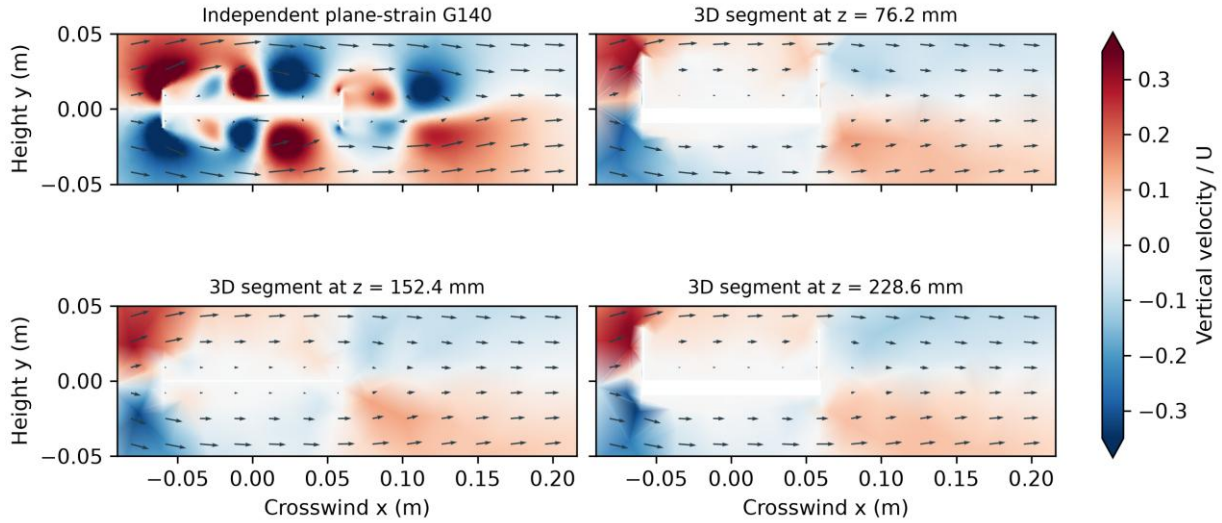

Figure 32. Vertical velocity and in-plane velocity arrows at 0.150 model s. Upper left, the independent finite-strain G140 run. The other panels intersect the three-dimensional moving air mesh with planes near each floor beam and midway between them. All four panels have identical coordinates and colour limits. Blank structural regions carry no fluid values.

Table 15. Local velocities from the finite-strain G140 section and the two-bay pilot at 0.150 model s, normalized by the inlet speed of 1.8 m/s.

Wake probe at x = 90 mm, y = 6 mm	Crosswind / U	Vertical / U	Spanwise / U
Independent 2D	−0.242	+0.221	0
3D, z = 76.2 mm	+0.189	−0.0003	+0.0208
3D, z = 152.4 mm	+0.222	−0.0279	−0.0219
3D, z = 228.6 mm	+0.256	−0.0200	−0.0107

At the probe the planar fluid is recirculating while all three segment stations have positive crosswind velocity. In three dimensions fluid can turn along the span and carry momentum between neighbouring stations. Those motions and all span derivatives are suppressed in the planar solution. The near-wake velocity and the associated pressure distribution can therefore vary along the three-dimensional deck. Differences in local geometry, mesh resolution and supports also affect this comparison. One probe and one time cannot attribute the entire discrepancy to dimensionality.

The structural distinction is equally important. The planar deck can pitch in its own plane and can develop σ_{zz} through lateral restraint. Its spanwise shear strains vanish. A three-dimensional deck can warp, bend between floor beams and transfer twisting moment into the girder and hanger lines through longitudinal shear. A full-span aeroelastic prediction must additionally represent the towers, suspended span and the relative phase of motions across that span. The existing segment samples only two bays.

11.24 Following the load across the roadway

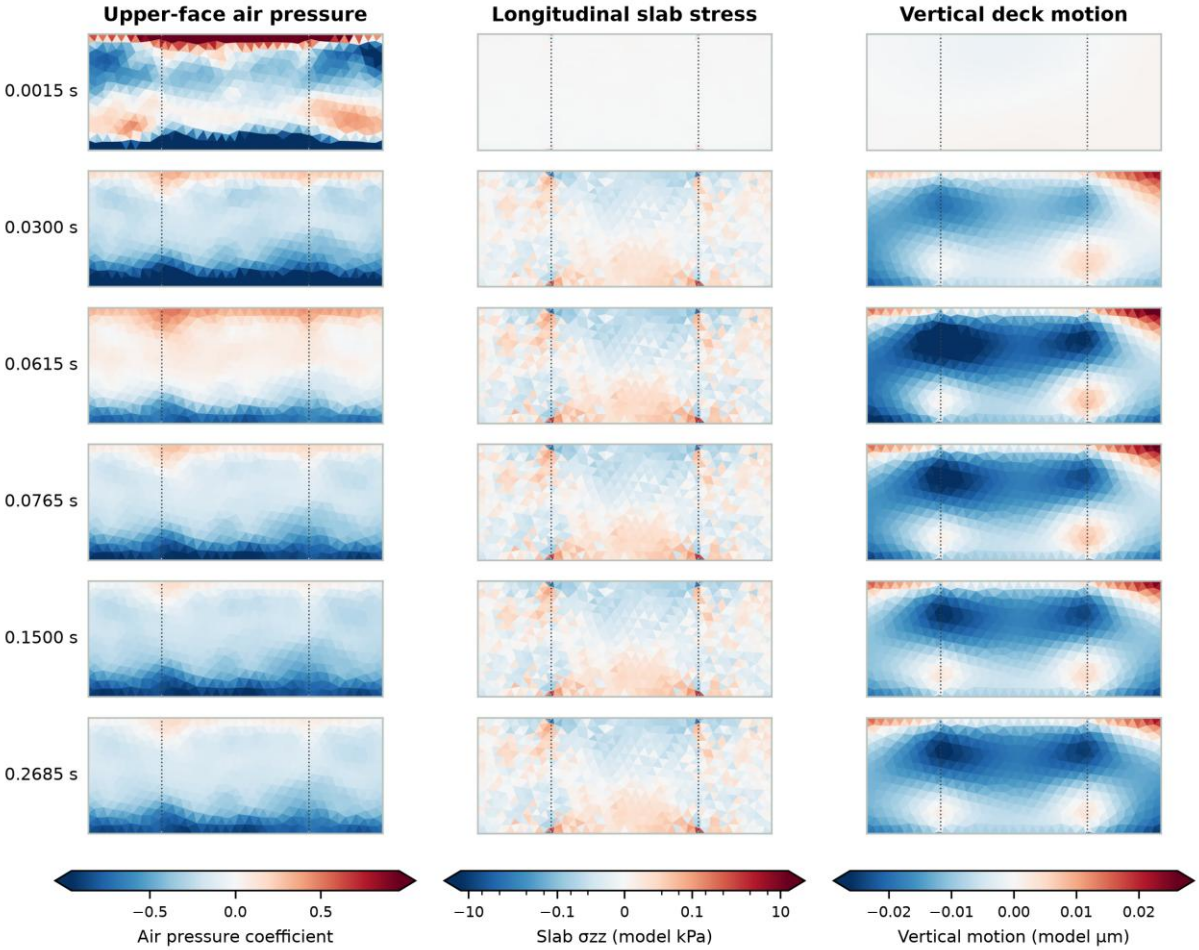

Figure 33. Plan views of the same exposed upper slab at six model times. From left to right, air pressure coefficient, signed longitudinal slab stress and vertical displacement. Span increases to the right and wind enters at the lower edge. Dashed station marks locate both floor beams. A column keeps its scale across all rows. The stress scale is symmetric and nonlinear to show the low-stress roadway together with the higher stresses at its edges.

The three maps share 878 triangular faces covering 0.036277 m^2 of model roadway. Girder tops and four link footprints are excluded. The fluid column uses face-averaged gauge pressure divided by the inlet dynamic pressure before the structural load ramp. The central column takes the stress of the adjoining concrete tetrahedron. Its sign distinguishes longitudinal tension from compression. The right column reports mean vertical nodal motion in micrometres. Pressure and displacement colours clip at the pooled 99th percentile of absolute post-ramp face values.

At 0.150 s the upper-surface pressure coefficient ranges from −0.996 to +0.169. The slab carries −7.32 to +11.78 kPa in the span direction, and vertical displacement ranges from −0.0329 to +0.0331 µm. Local stress maxima cluster near the girder lines at the second floor beam. Although the pressure acts normal to the road, compatibility with girders and transverse members produces a longitudinal slab response. The upper-surface pressure alone cannot recover total lift or moment. That requires the lower face, edge faces, wall shear and their lever arms as in Figure 22.

12 Findings and engineering interpretation

The engineering question is when the wind can begin to amplify small torsional disturbances. For the original deck we adopt a literature-based prototype onset estimate of 9.0 m/s, equivalent to 0.90 m/s at the present model scale. This is an aeroelastic hazard threshold. It does not specify a material failure load, a collapse time or a safe operating limit. Section 12.3 compares the damping criterion with a physical full-bridge model. The wind field and structural state on 7 November 1940 are outside the scope of the reconstruction.

The dry main-span model admits antisymmetric torsion at 1.8694 model Hz. Equal line moments at mirror stations cancel in the modal projection, leaving a relative residual of 4.8×10^{-15}. The archived forced response therefore misses the historical reversal of twist. In the isolated segment, opposite local moments coexist at a single instant. In the finite-strain section, pitch work changes sign between intervals on G140. These observations describe different ways wind loads act across space and time.

Across the eight shared startup frames, the four donor meshes produced patch tensile peaks of 6.75, 1.60, 1.97 and 1.29 kPa in order of refinement. The sequence is nonmonotonic. Only the pilot donor covers the full 2.685 s prototype interval. Its 17.42 kPa peak is therefore specific to that history and donor. The archived comparisons provide no mesh-converged peak, fatigue life or historical sequence of component failure.

12.1 Assessment against the stated criteria

Table 16. Outcomes against the interpretation criteria in Table 8. The spatial modes refer to the isolated segment. The last row uses the trial material and the long pilot history. Table 13 compares donor grids over the shorter startup window.

Quantity	Archived result	Interpretation
Fixed wake	G100 to G070 gives the same peak St and a 5.14% change in RMS lift.	The finest load comparison exceeds the 5% criterion.
Sectional pitch	Positive work in 3/3 finite-strain G200 intervals and 2/4 on G140.	Growth and an onset bracket remain unverified.
Dry spatial modes	Mode 4 has MAC 0.990 and a 13.4% frequency change relative to the fine mesh.	Mesh-to-mesh shape agreement exceeds 0.95. The frequency remains grid-sensitive.
Suspended span	Uniform loading gives the same twist sign at both quarter spans.	The prescribed-load test verifies symmetry. It cannot validate the historical mode transition.
Local concrete	Peak tension 17.42 kPa in 2.685 s. Damage is zero in all 6,144 cells.	Transfer is conservative for the sampled history. Crack initiation and softening were never activated.

12.2 Independent checks against the historical response

The federal Historic American Engineering Record gives two observations with distinct physical meanings. Before the change in motion, the deck oscillated vertically about 38 times per minute. During torsion, the record describes about 12 cycles per minute and a nearly stationary midpoint between two twisting lobes [9, p. 6]. These are observations under wind. The 1.875 model Hz dry benchmark used to select the insert stiffness shares structural inputs with the present model [3]. It measures calibration consistency only.

Table 17. Observations from the original bridge compared with archived outputs converted to prototype units. Frequency follows Eq. (1). Mode ordinates are drawn from results/span-modes.csv. The field history, mode shape and sectional transient represent different observables.

Observable	Independent record	Scaled result and assessment
Vertical response	About 38 cycles/min, or 0.63 Hz [9].	Moving G200 wake and lift peak at 0.656 Hz prototype equivalent. Neither is a measurement of deck heave. Lock-in remains unresolved.
Torsional timing	About 0.20 Hz [9]. Song et al. summarize a historical value near 0.23 Hz [3].	The linear G200 pitch-spectrum peak scales to 0.188 Hz. Three crossings span 0.175–0.197 Hz. Spectral resolution is about 0.083 Hz at full scale. The small frequency differences cannot validate a growth rate.
Spatial pattern	Opposed motion on the two sides of midspan, with a midpoint node [6, 9].	The first dry torsional mode has normalized quarter-span ordinates +1 and −1. The uniform-load solution gives equal-signed quarter-span twists and misses the observed pattern.
Rotation amplitude	The historical account reports inclinations up to about 45° [9].	At 18 m/s prototype-equivalent wind, the finer finite-strain section reaches 0.882°. Angle is scale invariant. The computed transient does not reproduce the large rotation.

The laboratory evidence and the historical record also have different limits. In a year-long natural-wind study, Li et al. observed large-amplitude flutter of a 1:8.53 full-bridge aeroelastic model [10]. This supplies an independent physical observation of the instability under variable wind. It gives no direct measurement of the local band moments, clamp stress or concrete-patch tension in this calculation. Those quantities retain the numerical verification status in Table 16.

12.3 Prototype critical wind speed

We define critical wind speed as the incident speed at which total modal damping passes through zero for small torsional motion. This definition distinguishes incipient instability from the later growth to damaging rotation. Among the available numerical estimates, the criterion is evaluated directly by Szabó et al. [4, Fig. 9]. Using large-eddy simulation on their fine mesh (2.5 million cells), they tracked quarter-span torsional decay at 5, 10 and 15 m/s, interpolated to zero total damping, and reported 9.0 m/s for the original-deck configuration. Song et al. [3] independently found 8 < Ucrit ≤ 9 m/s in a suspended-deck simulation. The reported bracket describes that study's tested speeds. It is not a statistical confidence interval for the actual bridge.

On that basis we adopt 9.0 m/s as a single prototype reference. With the length ratio $\lambda = 0.01$ and equal gravity, Eq. (1) gives $U_p = U_m/\sqrt{\lambda}$. The equivalent speed is 0.90 m/s on the present model, and $0.90/\sqrt{0.01} = 9.0$ m/s on the prototype. In the same scaling the nominal 1.8 m/s case represents 18 m/s. The upper reduced-speed bound in [3] gives the same model equivalent: 4 × 1.875 Hz × 0.120 m = 0.90 m/s. Here 1.875 Hz is the scaled dry frequency used in that comparison. The neutral-damping estimate comes from [4]. The scale conversion puts it and the present runs in common units and adds no independent evidence for onset.

A physical full-bridge model provides a check on the size of the discrepancy. Billah and Scanlan [6, p. 123, Fig. 3] report Farquharson's 1:50 full-model onset at 3.3 ft/s for the one-node torsional mode. Applying the speed factor $\sqrt{50}$ gives 15.91 mph, or about 7.1 m/s, at full scale. Their section-model analysis gives 18.6 mph (8.3 m/s) for an assumed mechanical damping ratio of 0.005 and 22.9 mph (10.2 m/s) at 0.010 [6, Table I]. These tests show why a single prototype value depends on the assumed damping. The published 9.0 m/s estimate exceeds the historical full-model onset by about 1.9 m/s.

The finer finite-strain TENSORA mesh was run at 1.8 m/s only. Its pitch work was positive in two of four crossing intervals. The three-speed sweep used the coarser linear section and yielded positive window-integrated pitch work at every speed. Neither record provides a sign change in total damping. The 17.0 and 18.8 m/s historical wind readings [2] place the bridge above the adopted reference on the morning of failure. They do not establish the speed of first instability. Reduced Reynolds number, uncertain damping and the absence of full-span aerodynamic feedback limit transfer of the computed amplitudes to the bridge.

12.4 Prototype-equivalent stresses

At equal gravity and fluid density, the velocity ratio is $\sqrt{\lambda}$ and the dynamic pressure ratio is λ, where $\lambda = 0.01$. Matching structural strain with $E_m/E_p = \lambda$ gives $\sigma_m/\sigma_p = \lambda$. Thus each model stress component, principal stress and von Mises stress scales by 100 from model to prototype. Strain and rotation are unchanged. One model kPa corresponds to 0.100 prototype MPa. The concrete patch was already solved in prototype units.

Table 18. Maxima over the available histories at 18 m/s prototype-equivalent wind. Tension is positive. The local 3D and patch records span 2.685 prototype s. The independent finite-strain G140 section spans 23.98 prototype s. Each row reports its own stress measure and sampling location.

Component and observable	Archived stress	Prototype stress	Prototype time
Steel upper link, recovered nodal von Mises maximum	79.13 kPa (model)	7.913 MPa	0.630 s
Roadway upper face, maximum longitudinal tension	+13.53 kPa (model)	+1.353 MPa	0.615 s
Roadway upper face, maximum longitudinal compression	−8.570 kPa (model)	−0.857 MPa	0.630 s
Equivalent 2D deck, maximum von Mises stress	8.678 kPa (model)	0.868 MPa	9.900 s
Plain-concrete patch, maximum principal tension	17.42 kPa (prototype)	0.01742 MPa	0.615 s

The highest recovered nodal equivalent stress in the 180 spatial frames is at the windward fixed cap of the first floor beam (Figure 25). It occurs at model step 42, with prototype coordinates x = −5.85 m, y = 3.50 m, z = 7.62 m. The neighboring cut gives 7.912 MPa at the same time. The idealized clamp concentrates stress. The agreement locates the concentration but cannot establish the as-built connection stress, yielding or rivet failure. The archive contains no verified steel yield strength for that connection.

The reported stresses are increments due to the applied aerodynamic history. Absolute service stresses would also require dead-load and pre-existing stresses at the same material points. The artificial planar support inserts have no historical material counterpart. The 9.0 m/s onset reference and these 18 m/s transient stresses address different states. Applying a squared wind-speed ratio to the latter would omit changes in motion and load phase.

12.5 Roadway stress and local damage assessment

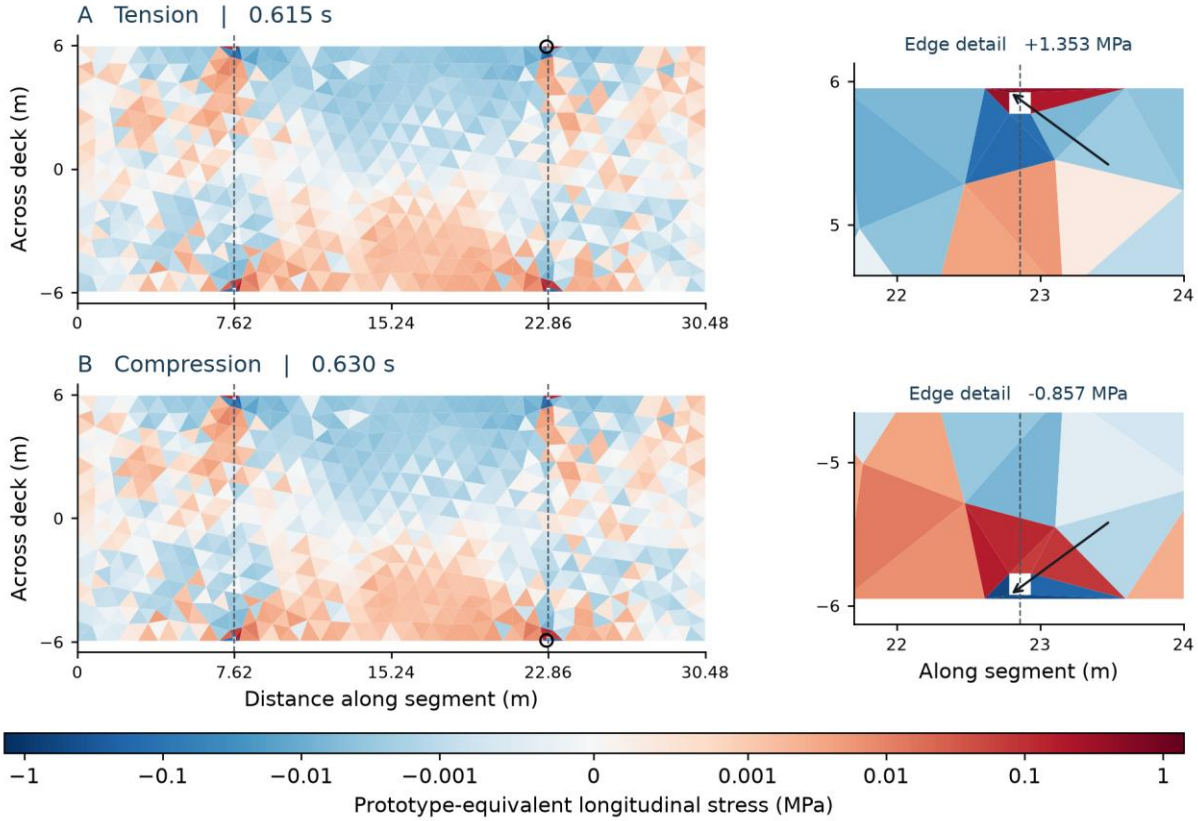

Figure 34. Prototype-equivalent longitudinal stress on the exposed upper roadway at the two recorded extreme states. Circles mark the governing face in each frame. Dashed lines locate the floor beams. Each detail enlarges the marked edge at the second floor beam. All panels share a signed logarithmic colour scale with a linear interval from −0.001 to +0.001 MPa. The maps use all 878 archived faces per frame.

Both extrema occur near the second floor beam, approximately 22.78 m from the segment cut and on opposite deck edges. The largest positive longitudinal component is 1.353 MPa. It is below the patch material's illustrative uniaxial tensile strength of 3 MPa. This single stress component cannot bound the maximum principal tension from above. The roadway's multiaxial cracking margin therefore remains undetermined. Its upper-surface stress at the second beam also samples a different location from the patch at the first beam.

At the first beam the OOFEM patch provides a direct material check. Its peak principal tension is 0.01742 MPa, or 0.581% of the trial tensile strength. All 6,144 elements retain zero damage. The recorded history therefore gives no tensile damage initiation in this patch. The steel cap and the opposite roadway edges at the second beam are the stress concentrations identified by the segment. Their historical capacities and total in-service stresses are unknown.

Stress data for Table 18 come from the native segment-series solid frames (Von_Mises_Stress, peak at solid_1_00042.vtk), the roadway frame_summary.csv, qa/material_fields/planar_response.csv and spatial/damage_trace.csv under results. The link cut history is in results/spatial/torque/cutaway_cap.csv.

References

[1] Washington State Department of Transportation. 1940 Narrows Bridge — The Machine. Span statistics, suspender spacing and 1940 road-deck drawing. https://wsdot.wa.gov/TNBhistory/1940-bridge.htm

[2] Washington State Department of Transportation. The Collapse. Historical chronology and reported local wind measurements, 7 November 1940. https://wsdot.wa.gov/TNBhistory/collapse.htm

[3] Song, D., Kim, W., Kwon, O.-K. and Choi, H. (2022). Vertical and torsional vibrations before the collapse of the Tacoma Narrows Bridge in 1940. Journal of Fluid Mechanics, 949, A11. https://doi.org/10.1017/jfm.2022.748

[4] Szabó, G., Györgyi, J. and Kristóf, G. (2020). Three-dimensional FSI simulation by using a novel hybrid scaling — application to the Tacoma Narrows Bridge. Periodica Polytechnica Civil Engineering, 64, 975–988. https://doi.org/10.3311/PPci.15586

[5] TENSORA v1.2.7. In-house computational mechanics platform. Release tag and archived source revision a910bde6fa43bae3224bbd0439e72d7e0e865452. https://github.com/Sakihandser/TENSORA/releases/tag/v1.2.7

[6] Billah, K. Y. and Scanlan, R. H. (1991). Resonance, Tacoma Narrows bridge failure, and undergraduate physics textbooks. American Journal of Physics, 59, 118–124. https://doi.org/10.1119/1.16590

[7] SU2 Foundation. SU2 8.6.0, compressible neo-Hookean stress implementation, nonlinear_models.cpp. https://github.com/su2code/SU2/blob/v8.6.0/SU2_CFD/src/numerics/elasticity/nonlinear_models.cpp

[8] OOFEM. Material Library Manual, isotropic damage model for tensile failure (idm1). https://www.oofem.org/resources/doc/matlibmanual/html/pages/material-models-for-tensile-failure.html

[9] Hadlow, R. W. (1993). Tacoma Narrows Bridge. Historic American Engineering Record, HAER No. WA-99, p. 6. National Park Service. Library of Congress. https://tile.loc.gov/storage-services/master/pnp/habshaer/wa/wa0400/wa0453/data/wa0453data.pdf

[10] Li, Q., Zhang, M., Xu, F., Wang, P., Ma, Z. and Yu, H. (2026). Flutter of the Old Tacoma Narrows Bridge model in natural winds: Long-term experiments and statistical analysis. Engineering Structures, 365, 123219. https://doi.org/10.1016/j.engstruct.2026.123219

Data availability and AI use

The accompanying supplementary files contain model definitions, applied case settings, processed time histories, selected native fields and result videos. The SHA-256 manifests identify the distributed files. README.txt in Supplementary File 1 describes how to combine the archives and identifies the native outputs retained separately.

OpenAI Codex was used to translate and polish the language, visualize the computational results, and edit the layout and formatting of this technical report.

Author contributions

Mingze Hong. Software, Methodology (model development), Formal analysis (numerical simulation and data analysis), and Writing – original draft.

Bojun Yang. Investigation (literature collection), Data curation (parameter compilation), and Writing – review & editing (fact-checking and revision).

Declarations

Funding. The authors received no funding for this work.

Competing interests. The authors declare no competing interests.

Supplementary Files

This is a list of supplementary files associated with this preprint. Click to download.

- SupplementaryFile1Resultsandvideos.zip
- SupplementaryFile2Planarandstripmodels.zip
- SupplementaryFile3Spatialandcomponentmodels.zip